


RESEARCH ARTICLE

10.1029/2019MS001875

Special Section:

Carbon and Weather: Results from the Atmospheric Carbon and Transport -- America Mission

Key Points:

- The simulation is evaluated using CONUS-scale, long-term data, and in situ measurements that resolve the structures of midlatitude cyclones
- WRF-VPRM is shown to reproduce the structures in CO₂ mole fractions observed within midlatitude cyclones
- From May to September, biogenic fluxes dominate variability in XCO₂ over most of the CONUS except around a few metropolitan areas such as LA

Supporting Information:

- Supporting Information S1

Correspondence to:

X.-M. Hu,
xhu@ou.edu

Citation:

Hu, X.-M., Crowell, S., Wang, Q., Zhang, Y., Davis, K. J., Xue, M., et al. (2020). Dynamical Downscaling of CO₂ in 2016 Over the Contiguous United States Using WRF-VPRM, a Weather-Biosphere-Online-Coupled Model. *Journal of Advances in Modeling Earth Systems*, 12, e2019MS001875. <https://doi.org/10.1029/2019MS001875>

Received 20 AUG 2019

Accepted 4 MAR 2020

Accepted article online 11 MAR 2020

Dynamical Downscaling of CO₂ in 2016 Over the Contiguous United States Using WRF-VPRM, a Weather-Biosphere-Online-Coupled Model

Xiao-Ming Hu^{1,2} , Sean Crowell² , Qingyu Wang² , Yao Zhang^{3,4} , Kenneth J. Davis^{5,6} , Ming Xue^{1,2} , Xiangming Xiao³ , Berrien Moore² , Xiaocui Wu³ , Yonghoon Choi⁷ , and Joshua P. DiGangi⁷

¹Center for Analysis and Prediction of Storms, Norman, OK, USA, ²School of Meteorology, University of Oklahoma, Norman, OK, USA, ³Department of Microbiology and Plant Biology, and Center for Spatial Analysis, University of Oklahoma, Norman, OK, USA, ⁴Now at Department of Environmental Engineering, Columbia University, New York, NY, USA, ⁵Department of Meteorology and Atmospheric Science, University Park, PA, USA, ⁶Earth and Environmental Sciences Institute, The Pennsylvania State University, University Park, PA, USA, ⁷NASA Langley Research Center, Hampton, VA, USA

Abstract Ecosystem function (particularly CO₂ fluxes and the subsequent atmospheric transport), synoptic-scale weather (e.g., midlatitude cyclones), and interactions between ecosystems and the atmosphere can be investigated using a weather-biosphere-online-coupled model. The Vegetation Photosynthesis and Respiration Model (VPRM) was coupled with the Weather Research and Forecasting (WRF) model in 2008 to simulate “weather-aware” biospheric CO₂ fluxes and subsequent transport and dispersion. The ability of the coupled WRF-VPRM modeling system to simulate the CO₂ structures within midlatitude cyclones, however, has not been evaluated due to the lack of data within these weather systems. In this study, VPRM parameters previously calibrated off-line using eddy covariance tower data over North America are implemented into WRF-VPRM. The updated WRF-VPRM is then used to simulate spatiotemporal variations of CO₂ over the contiguous United States at a horizontal grid spacing of 12 km for 2016 using an optimized downscaling configuration. The downscaled fields are evaluated using remotely sensed data from the Orbiting Carbon Observatory-2, Total Carbon Column Observing Network, and in situ aircraft measurements from Atmospheric Carbon and Transport-America missions. Evaluations show that WRF-VPRM captures the monthly variation of column-averaged CO₂ concentrations (XCO₂) and episodic variations associated with frontal passages. The downscaling also successfully captures the horizontal CO₂ gradients across fronts and vertical CO₂ contrast between the boundary layer and the free troposphere. WRF-VPRM modeling results indicate that from May to September, biogenic fluxes dominate variability in XCO₂ over most of the contiguous United States, except over a few metropolitan areas such as Los Angeles.

Plain Language Summary Global warming due to increase in greenhouse gases, particularly CO₂, is well known as a critical issue facing humanity. CO₂ concentration increased quickly over the past two centuries, with the overall trend largely due to fossil fuel emissions. Year-to-year variations in CO₂ growth rate are not well understood, which is partially due to uncertainty in terrestrial CO₂ fluxes. Accurate estimation of terrestrial CO₂ fluxes is limited by land cover and land use changes, drought, and weather influences. These factors/processes and their impact on CO₂ fluxes and atmospheric mole fractions can be investigated using a weather-biosphere-online-coupled model. The Vegetation Photosynthesis and Respiration Model (VPRM) coupled with the Weather Research and Forecasting (WRF) model (referred to as WRF-VPRM) is one such tool. In this study, optimal VPRM parameters are implemented into WRF-VPRM. The updated WRF-VPRM is then used to simulate CO₂ mole fractions over the United States for 2016. The simulation is evaluated using aircraft measurements and remote sensing data. Evaluations show that WRF-VPRM captures the temporal variation of CO₂ concentrations, as well as the horizontal CO₂ gradients across fronts and vertical CO₂ contrast in the low troposphere. Simulations using this modeling system can be used to help understand regional to global CO₂ budgets.

© 2020. The Authors.

This is an open access article under the terms of the Creative Commons Attribution License, which permits use, distribution and reproduction in any medium, provided the original work is properly cited.

1. Introduction

Sources and sinks of CO₂ at regional to continental scales remain poorly understood. Terrestrial ecosystems exhibit significant spatial and temporal variability in CO₂ fluxes, directly affecting the atmospheric CO₂ growth rate. Data- and process-driven models show large differences in the spatial-temporal mean and variability patterns of gross primary production (GPP) (Anav et al., 2015), especially in the semiarid regions (Y. Zhang, Xiao, Jin, et al., 2016). Hilton et al. (2014) showed that large uncertainties exist in a terrestrial CO₂ flux model calibrated to North American flux towers as a result of ambiguity regarding the optimal choices for parameters. Huntzinger et al. (2018) have shown large divergence in terrestrial biosphere CO₂ flux models driven by model structural differences. Raczka et al. (2013) showed relatively poor seasonal and interannual performance of terrestrial CO₂ flux models when compared to North American eddy covariance flux towers. In semiarid ecosystems, although the spatial patterns of CO₂ fluxes are often explained by the variation of water availability, biotic meristem growth potential, and their interactions (Knapp & Smith, 2001), the pulse, seasonal, and interannual dynamics of vegetation and the underlying mechanism and the subsequent impact on CO₂ fluxes are not well understood, which hinders a better understanding of sources and sinks of CO₂ at regional to global scales. Large uncertainties in biogenic CO₂ flux estimates from certain ecosystems (e.g., semiarid ecosystems) at regional scales cause significant uncertainties in the estimation and projection of the global terrestrial carbon cycle (Reichstein et al., 2013).

Regional-scale CO₂ fluxes are widely affected by land cover and land use changes (e.g., deforestation, reforestation, woody plant encroachment, and cropland expansion) (Lark et al., 2017; Wang et al., 2017), drought (Zhou et al., 2017), and synoptic-scale weather (e.g., cyclones at midlatitudes). Over the past 50 years, an enhanced seasonal exchange of CO₂ has been observed in the Northern Hemisphere (Graven et al., 2013), which was interpreted as increasing GPP in northern ecosystems induced by CO₂ fertilization, extended growing seasons, and nitrogen deposition (Baldocchi et al., 2016; Forkel et al., 2016; Graven et al., 2013) as well as amplification of agricultural productivity in northern midlatitudes (Miles et al., 2012; N. Zeng et al., 2014). With the increasing frequency of extreme climate events (Easterling et al., 2000), the interannual variability of GPP is also projected to increase (Zscheischler et al., 2014) and will cause significant impacts on the global terrestrial carbon cycle. Regional CO₂ mole fractions, used to infer regional fluxes via atmospheric inversions (Lauvaux et al., 2012), are difficult to simulate due both to the interactions between weather and surface fluxes and considerable sensitivity to variations in atmospheric transport (Diaz-Isaac et al., 2018; Diaz-Isaac et al., 2014). Midlatitude weather systems cause large fluctuations in atmospheric CO₂ (Hurwitz et al., 2004) and play a major role in regional and global CO₂ transport (Chan et al., 2004; Parazoo et al., 2011). All of these processes can be investigated using a weather-biosphere-coupled CO₂ model that considers the feedbacks between synoptic weather and land surface dynamics. Development of such systems has been started in the past few decades. In 2008, the Vegetation Photosynthesis and Respiration Model (VPRM) (Mahadevan et al., 2008; Xiao et al., 2004) was coupled into the Weather Research and Forecasting (WRF) model to simulate “weather-aware” biospheric CO₂ fluxes (in addition to anthropogenic CO₂ emissions) and their subsequent atmospheric transport/dispersion (Ahmadov et al., 2007). This online coupled system (referred to as WRF-VPRM) can be used to investigate the impact of the weather-informed land surface dynamics on the spatiotemporal variability of atmospheric CO₂ fluxes and concentrations. The online systems simulate meteorology and chemistry (or tracers) simultaneously in one coordinate frame, as opposed to off-line systems in which meteorological analysis/simulation is conducted prior to the simulation of chemistry (or tracer transport) (Hu, 2008).

Evaluation of WRF-VPRM to date has been limited either to comparisons with spatially sparse observation networks (or to urban domains) or with short-term measurements. Early studies of WRF-VPRM development/application (Ahmadov et al., 2007; Ahmadov et al., 2009; Pillai et al., 2011) tested the system in a few case studies and with sparse tower measurements over small sub-Europe domains. A few published studies (Diao et al., 2015; Feng et al., 2016; Liu et al., 2018; Park et al., 2018) have applied WRF-VPRM to other continents. Diao et al. (2015) evaluated WRF-VPRM using surface CO₂ observations at three sites during a 5-day period in 2010 over eastern China, and Liu et al. (2018) evaluated WRF-VPRM using the greenhouse gases observing satellite (GOSAT) retrieved column-averaged CO₂ concentrations (XCO₂) over north China for 4 months in 2015; both Feng et al. (2016) and Park et al. (2018) applied WRF-VPRM to the

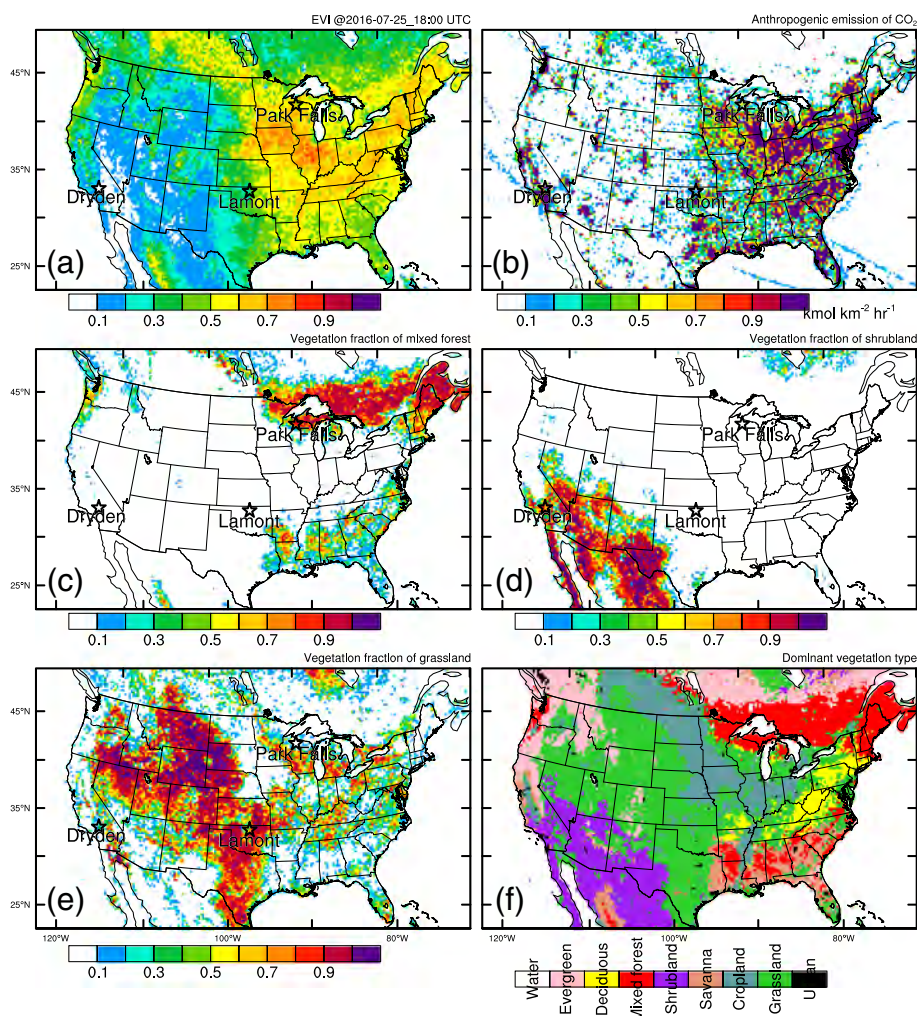


Figure 1. Major WRF-VPRM inputs including (a) EVI (25 July 2016 is displayed here as an example), (b) anthropogenic emission ($\text{kmol}\cdot\text{km}^{-2}\cdot\text{hr}^{-1}$) from the $0.1^\circ \times 0.1^\circ$ ODIAC, (c–e) vegetation fraction for mixed forest, shrubland, and grassland, and (f) dominant vegetation types including water, evergreen forest, deciduous forest, mixed forest, shrubland, savanna, cropland, grassland, and urban derived from MODIS data. Three TCCON sites (Park Falls [WI], Lamont [OK], and Dryden [CA]) are marked with stars.

Southern California Air Basin, which is strongly affected by anthropogenic CO_2 emissions and less affected by biogenic CO_2 fluxes. In Feng et al. (2016) and Park et al. (2018), accurate anthropogenic CO_2 emissions are most critical for accurate simulation of ambient CO_2 mixing ratios, while VPRM-simulated biogenic CO_2 fluxes play a less important role. Thus, WRF-VPRM was not stringently evaluated over the U.S. domain, particularly at scales of midlatitude weather systems. Lack of application and evaluation of WRF-VPRM over the U.S. domain is likely partially due to the sparsity of appropriate CO_2 measurements in the region, as well as the difficulty of interpreting model and observational mismatches in the atmospheric boundary layer due to poorly understood boundary layer dynamics (Díaz-Isaac et al., 2018; Díaz-Isaac et al., 2014). Some existing long-term observing networks do not have the necessary resolution to resolve the structures in atmospheric CO_2 mole fraction found within midlatitude weather systems.

A few more recent data sets, including the spaceborne XCO_2 data over the globe from the Orbiting Carbon Observatory-2 (OCO-2, Crisp et al., 2004; Crisp et al., 2008) since its launch in July 2014 and the in situ aircraft measurement over eastern United States in summer 2016 from the Atmospheric Carbon and Transport-America (ACT-America) mission (Digangi et al., 2018), provide an excellent opportunity to evaluate the WRF-VPRM regional model. The OCO-2 instantaneous high precision XCO_2 data have a 2.5-km^2

Table 1
Summary of the Configuration for WRF-VPRM Downscaling

Short wave radiation	Dudhia
Long wave radiation	Rapid radiative transfer model (RRTM)
Boundary layer	YSU
Microphysics	Morrison
Cumulus	Grell-3
Land surface model	NOAH
Vertical levels	47
Horizontal resolution	12 km × 12 km with 266 × 443 grid points
Time step	60 s
Meteorological initial and lateral boundary conditions	NCEP/DOE Reanalysis 2 (R2)
CO ₂ initial and lateral boundary conditions	CT2017 global simulation 3° × 2° outputs
Interior nudging variables	Spectral nudging horizontal wind components, temperature, and geopotential height
nudging coefficient	3 × 10 ⁻⁵ s ⁻¹
nudging height	above PBL
wave number	5 and 3 in the zonal and meridional directions, respectively
nudging period	throughout the downscaling simulation

horizontal resolution at nadir, enabling us to examine small-scale variability in column average CO₂. The ACT-America mission was designed to address the gap in observations and has enabled extensive observational documentation of the greenhouse gas distributions within midlatitude weather systems. The ACT-America summer 2016 field campaign used aircraft to collect comprehensive CO₂ and meteorological data in both boundary layer and free troposphere, and fair and frontal weather conditions over the eastern United States, enabling us to examine the three-dimensional spatial structure of CO₂ mole fraction within weather systems.

In this study, VPRM parameters optimized for North America (Hilton et al., 2013) are first incorporated into WRF-VPRM. The calibrated modeling system is then applied to simulate CO₂ fluxes and atmospheric CO₂ concentrations with a horizontal resolution of 12 km over contiguous United States (CONUS) for Year 2016 with the initial and boundary conditions of CO₂ from the CarbonTracker global simulation, Version CT2017 (Peters et al., 2007, with updates documented at <http://carbontracker.noaa.gov>). The WRF-VPRM downscaled outputs are evaluated using CONUS-scale, long-term remotely sensed observations (from OCO-2, and the Total Carbon Column Observing Network [TCCON]), as well as in situ measurements that resolve the internal structures of midlatitude cyclones (i.e., ACT-America).

The rest of this paper is organized as follows. Section 2 describes the WRF-VPRM model, downscaling configuration, optimized VPRM parameters, and evaluation data sets. Section 3 first presents meteorological evaluation, followed by a biogenic CO₂ flux comparison and XCO₂ evaluation, as well as individual contributions to XCO₂ from different sources, and finally closes with three case studies chosen from the ACT-America 2016 summer field campaign. Summary and discussion of future further improvement of WRF-VPRM is given in section 4.

2. Modeling Approach and Evaluation Data

2.1. Online Coupled Weather-Biosphere Model WRF-VPRM

VPRM simulates the net ecosystem exchange (NEE) of CO₂ through separate parameterizations for ecosystem respiration (ER) and gross ecosystem exchange (GEE) (Mahadevan et al., 2008):

$$\text{NEE} = \text{ER} - \text{GEE} \quad (1)$$

$$\text{ER} = \alpha \times T + \beta \quad (2)$$

$$\text{GEE} = \lambda \times T_{scale} \times W_{scale} \times P_{scale} \times FAPAR_{PAV} \times PAR \times \frac{1}{1 + \frac{PAR}{PAR_0}} \quad (3)$$

The two parameters α and β are used to model ER as a function of environmental temperature T . λ is the maximum light use efficiency ($\mu\text{mol CO}_2/\mu\text{mol photosynthetic photon flux density}$). T_{scale} , W_{scale} , and P_{scale} account for effects of temperature, water stress, and leaf age on photosynthesis, respectively. $FAPAR_{PAV}$ is the fraction of photosynthetically active radiation (PAR, $\mu\text{mol m}^{-2} \cdot \text{s}^{-1}$) absorbed by the photosynthetically active portion of the vegetation (PAV), which roughly equals the enhanced vegetation index (EVI); PAR_0 is the half-saturation value. Moderate Resolution Imaging Spectroradiometer (MODIS)-derived temporally invariant vegetation fractions (Figures 1c–1e), 8-day updated EVI (Figure 1a), and 8-day updated Land Surface Water Index (encoded in the water scalar, W_{scale}) are prescribed.

The VPRM is coupled at every model time step with the WRF model, which provides shortwave downward radiation and 2-m temperature to VPRM, which returns fluxes of CO₂ to be transported/dispersed by the WRF-simulated meteorological fields including winds and turbulence (Ahmadov et al., 2007). Note that in

Table 2
Parameter Values Used in This Study

	Evergreen forest	Deciduous Forest	Mixed forest	Shrub	Savanna	Crop	Grass
PAR_0	745.306	514.13	419.5	590.7	600	1074.9	717.1
λ	0.13	0.1	0.1	0.18	0.18	0.085	0.115
α	0.1247	0.092	0.2	0.0634	0.2	0.13	0.0515
β	0.2496	0.843	0.27248	0.2684	0.3376	0.542	-0.0986

Note. Units for parameters are as follows: λ : $\mu\text{mol CO}_2 \cdot \text{m}^{-2} \cdot \text{s}^{-1} / \mu\text{mol PAR} \cdot \text{m}^{-2} \cdot \text{s}^{-1}$; α : $\mu\text{mol CO}_2 \cdot \text{m}^{-2} \cdot \text{s}^{-1} \cdot ^\circ\text{C}^{-1}$; β : $\mu\text{mol CO}_2 \cdot \text{m}^{-2} \cdot \text{s}^{-1}$; PAR_0 : $\mu\text{mol PAR} \cdot \text{m}^{-2} \cdot \text{s}^{-1}$.

the current WRF-VPRM system, the effect of simulated CO_2 variations on radiation and subsequent weather is not considered. Instead, a climatological CO_2 concentration (379 ppmv) is used in the radiation scheme. Thus, the current WRF-VPRM system is, in a sense, not fully two-way coupled. However, the effect of CO_2 variations on radiation is minor compared to variations of moisture and clouds for relatively short time periods less than a decade, such as in our study.

Climatological monthly ocean CO_2 fluxes (Takahashi et al., 2009) based on sea surface partial pressure measurements are included in the WRF-VPRM simulations, and they are downloaded from https://www.ideal.columbia.edu/res/pi/CO2/carbon dioxide/pages/air_sea_flux_2000.html. Previous regional WRF-VPRM simulations (e.g., Feng et al., 2016; Park et al., 2018) illustrated that good-quality anthropogenic emissions are critical to reproduce surface CO_2 as well as XCO_2 over large metropolitan areas such as those found in the Southern California air basin. Two sets of anthropogenic CO_2 emission were tested with WRF-VPRM: One is taken from the Emission Database for Global Atmospheric Research (EDGAR, Petrescu et al., 2012) Version 4.2, which was used in a previous WRF-VPRM simulation over China (Diao et al., 2015), and the other is the Open-Data Inventory for Anthropogenic Carbon dioxide (ODIAC) emission (Oda et al., 2018) version 2018 (Figure 1b). Our evaluation of WRF-VPRM sensitivity simulations with the two emissions indicates that ODIAC leads to better performance in the CO_2 simulation, particularly around large urban areas. For metropolitan areas such as Los Angeles where anthropogenic fluxes dominate, CO_2 model bias can be mostly attributed to uncertainties in anthropogenic emissions (Feng et al., 2016). With the EDGAR anthropogenic emissions, WRF-VPRM significantly overestimates XCO_2 at the Caltech TCCON site by 3.2 ppmv (not shown), while using the ODIAC emission, the agreement between TCCON and WRF-VPRM in terms of XCO_2 at Caltech is much improved (see more discussion in section 3.3.1). Thus, only the results from WRF-VPRM simulation with the ODIAC emissions are shown in this manuscript.

2.2. Dynamical Downscaling Technique

CO_2 downscaling simulations with the WRF (Version 3.9.1.1)-VPRM model were conducted for Year 2016 at a 12-km grid spacing over the CONUS domain (see Figure 1) with the National Centers for Environmental Prediction-Department of Energy (NCEP/DOE) R2 data (Kanamitsu et al., 2002) providing meteorological initial and boundary conditions and the CT2017 global simulation $3^\circ \times 2^\circ$ outputs (Peters et al., 2007) providing CO_2 initial and boundary conditions. Note that CT2017 also provides $1^\circ \times 1^\circ$ concentrations over North America. To make sure the CT2017 model data fully cover our model domain and facilitate potential future comparison with our other WRF-VPRM downscaling simulations over China (Li et al., 2020), the $3^\circ \times 2^\circ$ global outputs were used. The WRF-VPRM downscaling simulation ran continuously from 1 January and ended on 31 December 2016. Long-term climate downscaling is challenging, particularly over certain regions in CONUS during warm months, likely due to complex impacts of unique local topography and other factors (X. Sun et al., 2016). We adopted the WRF dynamic downscaling configurations of our previous studies (Hu et al., 2017; Hu, Xue, et al., 2018) that have been shown to produce accurate downscaled climate over CONUS. The model domain has 47 vertical layers extending from the surface to 10 hPa. Table 1 lists the WRF model configurations, which include the Dudhia shortwave radiation scheme (Dudhia, 1989), the rapid radiative transfer model (Mlawer et al., 1997) for longwave radiation, the Noah land surface model (F. Chen & Dudhia, 2001), the Grell-3 cumulus scheme (Grell & Devenyi, 2002), the Morrison microphysics scheme (Morrison et al., 2009), and the Yonsei University planetary boundary layer (PBL) scheme. We also

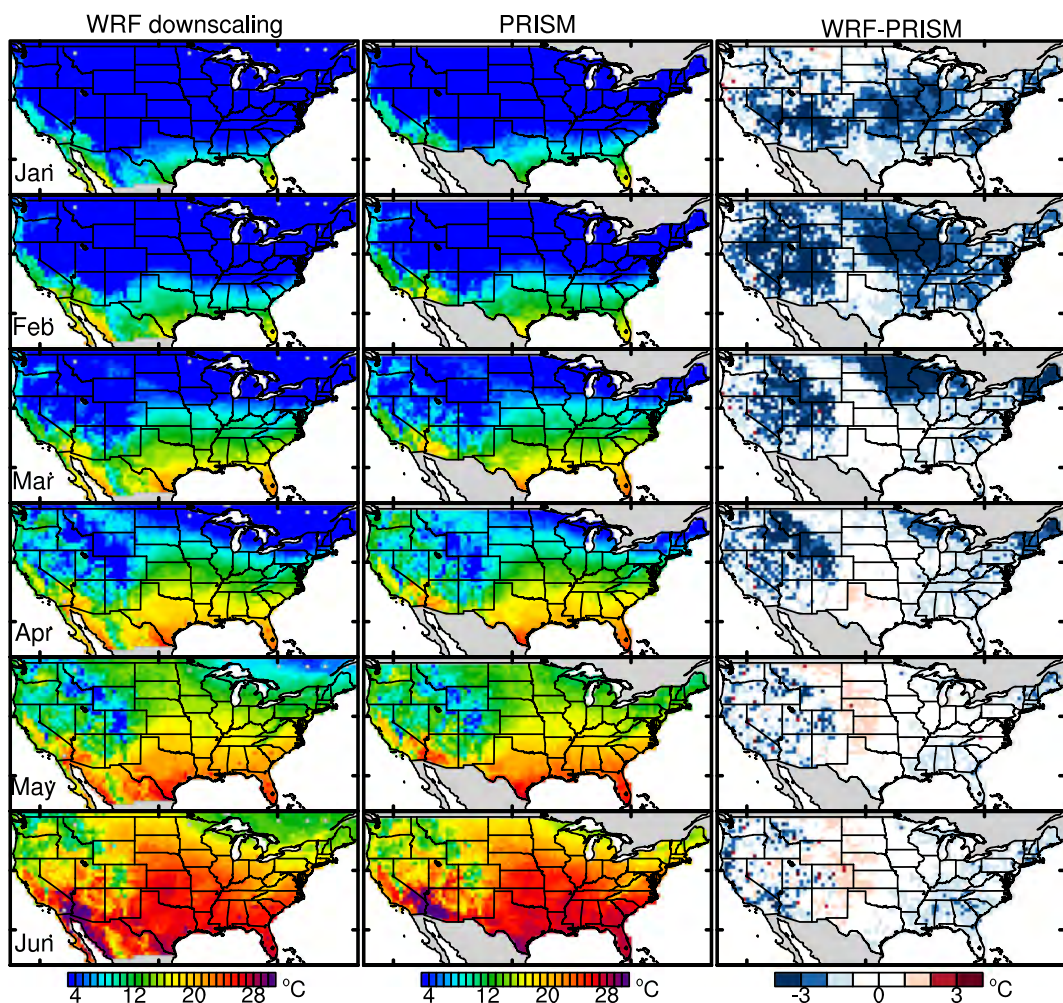


Figure 2. Monthly mean temperature at 2 m above the ground (left) downscaled by WRF, (middle) retrieved from the PRISM data, and (right) WRF bias (WRF-PRISM) for months (top to bottom) January through June.

tested the Mellor-Yamada-Janjic (MYJ) scheme (Janjic, 1994; Janjić, 1990) and found that MYJ generally underestimates the PBL heights during daytime, consistent with many previous evaluation (e.g., Hu et al., 2010; Hu et al., 2012; Hu et al., 2013). When CO₂ uptake due to photosynthesis process occurs in presence of a low PBL, CO₂ concentration in PBL decreases quickly during daytime. Too low PBL heights simulated by MYJ lead to too low CO₂ in the PBL (see one example in Figure S1 in the supporting information). Thus, we only show results with the Yonsei University scheme in this paper.

Importantly, spectral nudging for horizontal wind components, temperature, and geopotential height is applied, which has proven critical for accurate climate downscaling over CONUS (Hu, Xue, et al., 2018). We apply the spectral nudging configurations suggested by Wang and Kotamarthi (2014) for their WRF-based regional climate downscaling. Particularly, we adopted nudging wave numbers of 5 and 3 in the zonal and meridional directions over CONUS, respectively, thus nudging long waves with wavelengths of ~1,000 km to those of the driving fields from NCEP/DOE R2. The suggested nudging coefficient of $3 \times 10^{-5} \text{ s}^{-1}$ is adopted, corresponding to an ~9-hr *e*-folding damping time scale.

2.3. Updating the Four VPRM Parameters for Each Vegetation Type

In VPRM, land surface is classified into seven vegetation types based on MODIS data, that is, evergreen forest, deciduous forest, mixed forest, shrubland, savanna, cropland, and grassland, with independent parameters (i.e., α , β , λ , and PAR_0) for each type. The dominant type for each grid box is displayed in

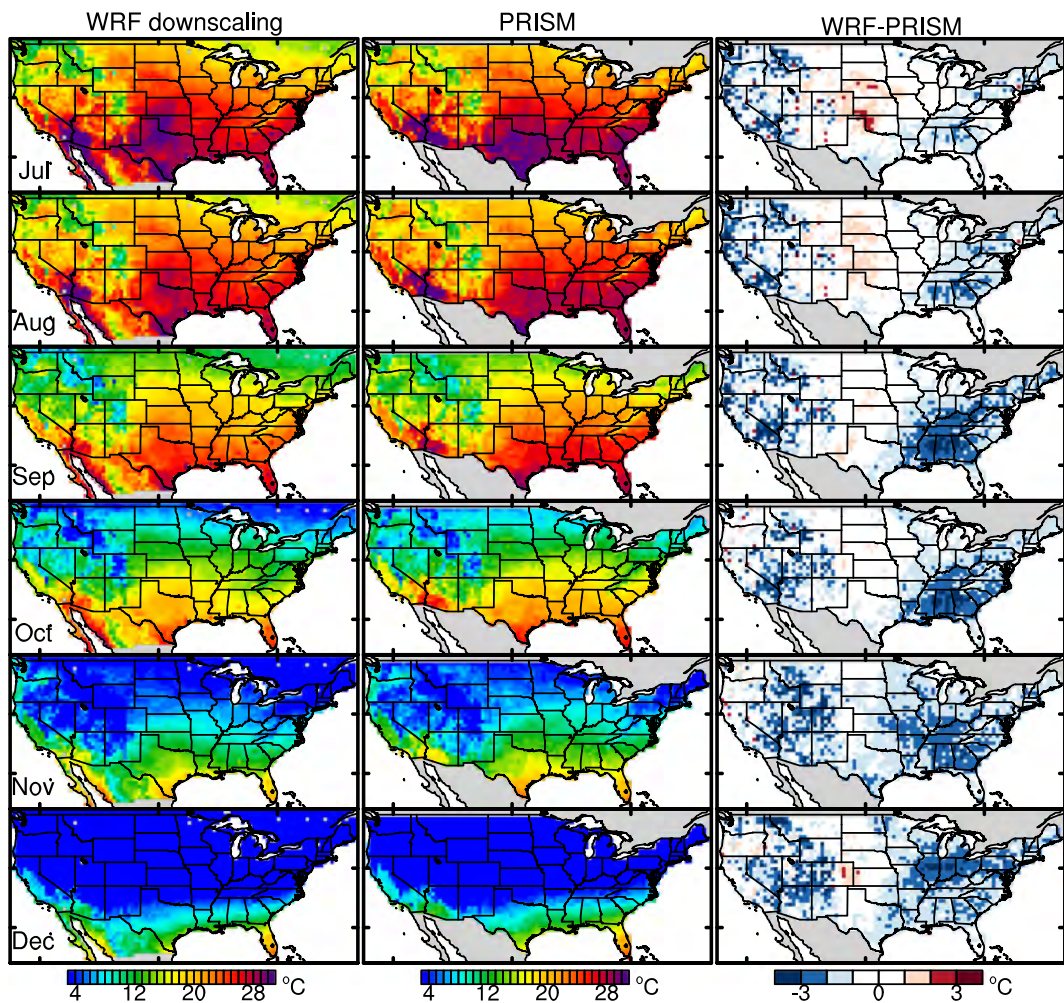


Figure 3. Same as Figure 2 but for months (top to bottom) July through December.

Figure 1f. The four parameters (i.e., α , β , λ , and PAR_0) used in the default WRF-VPRM were not objectively calibrated for the CONUS domain, which may lead to bias of simulated CO₂. In a test downscaling simulation, we noticed that the default WRF-VPRM significantly overestimates boundary layer CO₂ over the Appalachian Mountains, where deciduous forest dominates (figure not shown). After doubling PAR_0 for deciduous forest (making it comparable to that for savanna), WRF-VPRM shows a better performance over the Appalachian Mountains (Hu, Zhang, et al., 2018). These testing numerical experiments indicate that the default WRF-VPRM model parameters are suboptimal for CONUS, and so using calibrated

Table 3

Evaluation Statistics for Simulated Monthly Mean Temperature at 2 m AGL (T2) Against the PRISM Data in Each Month

Month	1	2	3	4	5	6	7	8	9	10	11	12
Mean obs (°C)	-0.4	3.5	7.9	11.2	15.3	21.6	23.6	22.8	19.2	13.9	8.6	0.0
Mean sim (°C)	-2.2	1.1	6.3	10.0	14.9	21.1	23.1	22.1	18.1	12.8	7.1	-1.3
r	0.98	0.98	0.98	0.98	0.97	0.97	0.96	0.96	0.97	0.98	0.98	0.99
MB (°C)	-1.7	-2.4	-1.6	-1.3	-0.4	-0.5	-0.5	-0.7	-1.2	-1.1	-1.5	-1.3
MAGE (°C)	1.8	2.4	1.7	1.4	0.9	1.0	1.0	1.1	1.3	1.2	1.5	1.5
RMSE (°C)	2.1	2.8	2.2	1.9	1.2	1.3	1.4	1.4	1.7	1.5	1.8	1.7
NMB (percent)	381.7	-68.5	-20.1	-11.2	-2.8	-2.5	-2.1	-3.0	-6.1	-7.9	-17.2	9,055

Note. The metrics include correlation coefficient r , mean bias (MB), mean absolute gross error (MAGE), root-mean-square error (RMSE), and normalized mean bias (NMB). Their formula can be found in Seigneur et al. (2000).

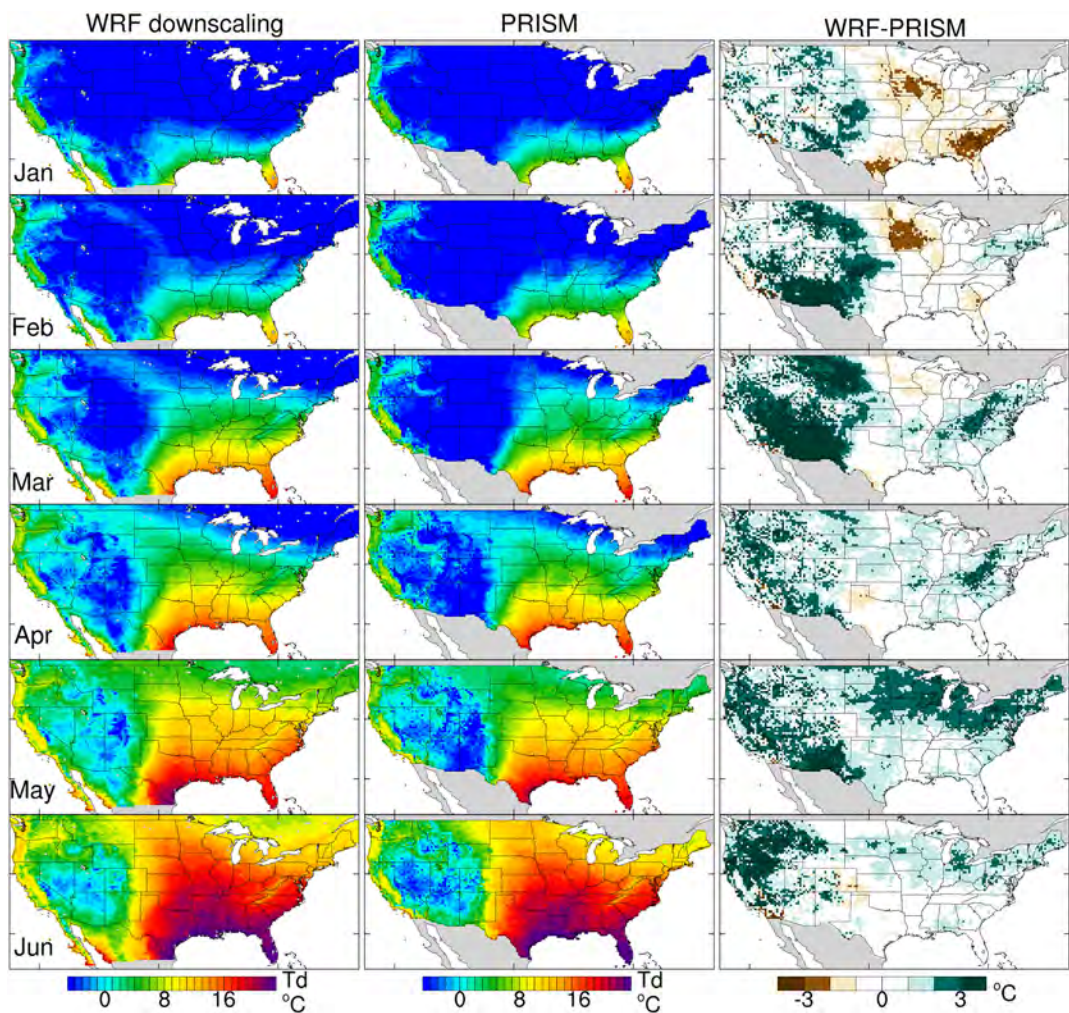


Figure 4. Monthly mean dewpoint (T_d) at 2 m above the ground (left) downscaled by WRF, (middle) retrieved from the PRISM data, and (right) WRF bias (WRF-PRISM) for months (top to bottom) January through June.

parameters over the CONUS domain is desired for the purpose of this study. Hilton et al. (2013) used observed NEE from a group of 65 eddy covariance tower sites over North America to calibrate VPRM parameters for different vegetation types (Hilton et al., 2016). These calibrated VPRM parameters (the median values in Figure 3 of Hilton et al. (2013)) are incorporated into WRF-VPRM in this study. Note that the default WRF-VPRM used shortwave radiation to drive VPRM (Mahadevan et al., 2008), while Hilton et al. (2013) used PAR to drive VPRM in his calibration. Using different variables to drive VPRM would affect the eventually calibrated VPRM parameters. To make Hilton et al.'s (2013) parameters compatible, VPRM in WRF is updated to be driven by PAR, which is calculated using (Mahadevan et al., 2008)

$$PAR = SW/0.505. \quad (4)$$

with PAR in $\mu\text{mol}\cdot\text{m}^{-2}\cdot\text{s}^{-1}$ and SW in W/m^2 . The implemented VPRM parameters are summarized in Table 2. In addition, T_{scale} , W_{scale} , and P_{scale} are updated to be confined between 0 and 1 to be consistent with the original design of Xiao et al. (2004). The reported WRF-VPRM downscaling results in this manuscript use this updated VPRM.

2.4. CO₂ Evaluation Data: OCO-2, TCCON, and ACT-America Aircraft

The downscaled CO₂ fields will be evaluated using a plethora of data, including remotely sensed data from TCCON, OCO-2, and in situ ACT-America aircraft data. A brief description of these data is provided below.

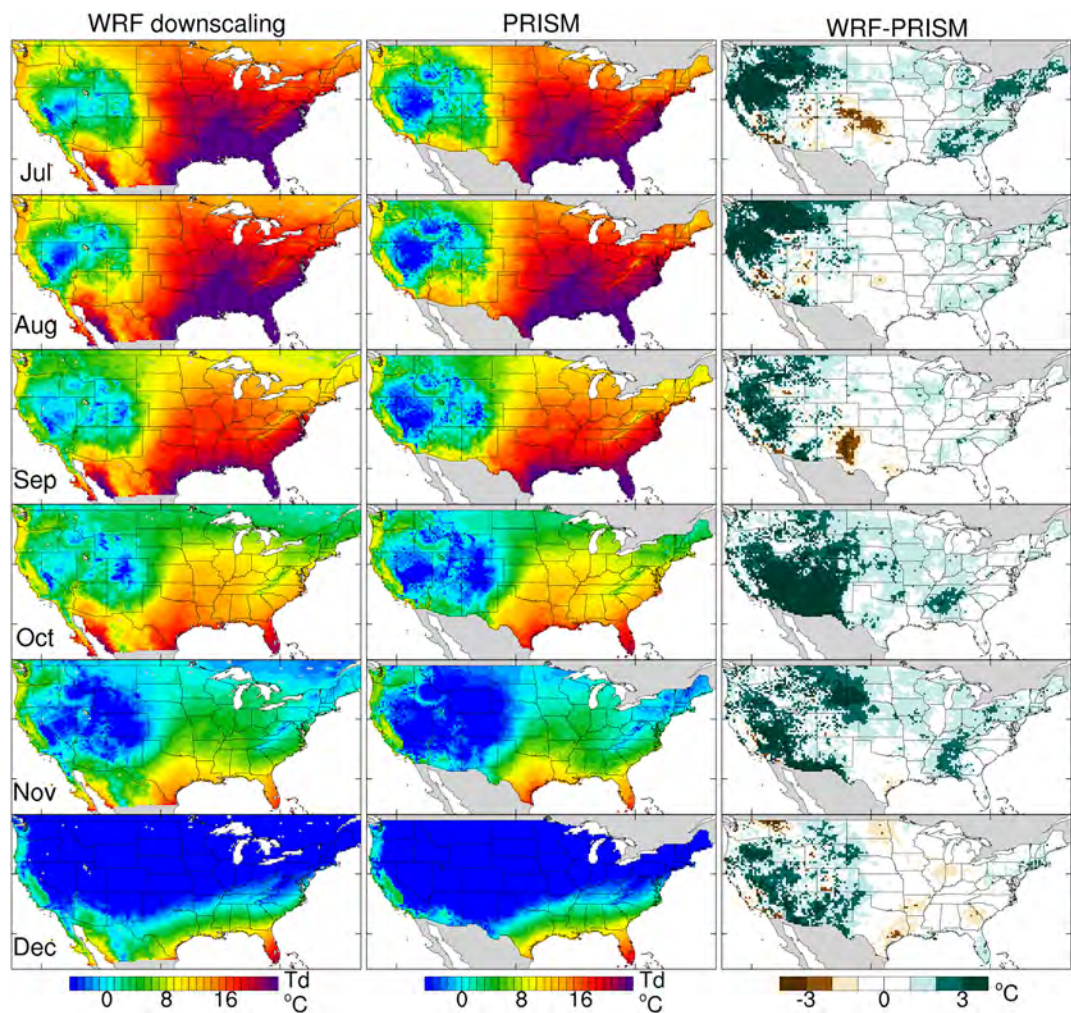


Figure 5. Same as Figure 4 but for months (top to bottom) July through December.

2.4.1. OCO-2

The OCO-2 satellite (Eldering et al., 2017) was launched in 2014 and has been collecting data for more than 4 years in a Sun-synchronous orbit with a local overpass solar time of about 1:30 p.m. OCO-2 measures reflected sunlight in three bands, and the resultant spectra are used to infer column average dry air mole fractions of CO₂, typically denoted by XCO₂. In addition to XCO₂, OCO-2 retrieves a number of other atmospheric parameters such as surface pressure and gross characteristics for multiple aerosol species. The data are bias corrected and filtered using ancillary retrieved parameters (Wunch et al., 2017). In this work, we utilize the OCO-2 Version 9r (Kiel et al., 2019, retrieved from <https://co2.jpl.nasa.gov/#mission=OCO-2>), and only data with quality flag = 0 (i.e., “good”) are used for comparisons with model fields.

Table 4

Evaluation Statistics for the Simulated Monthly Mean Dewpoint (Td) at 2 m Above the Ground Against the PRISM Data in Each Month

Month	1	2	3	4	5	6	7	8	9	10	11	12
Mean obs (°C)	-5.8	-4.2	-0.8	1.9	5.8	10.6	12.4	12.4	9.7	5.3	0.6	-6.0
Mean sim (°C)	-5.7	-3.4	0.8	3.0	7.6	11.7	13.6	13.5	10.4	7.1	2.0	-5.5
<i>r</i>	0.96	0.94	0.97	0.99	0.99	0.99	0.98	0.98	0.99	0.96	0.98	0.98
MB (°C)	0.1	0.8	1.5	1.1	1.7	1.0	1.1	1.1	0.7	1.8	1.4	0.6
MAGE (°C)	1.2	1.4	1.8	1.3	1.8	1.3	1.5	1.3	1.1	1.8	1.5	1.1
RMSE (°C)	1.5	1.9	2.3	1.5	2.0	1.7	2.0	1.9	1.4	2.5	1.8	1.4
NMB (fraction)	-1.9%	-19.5%	-202.4%	59.5%	30.0%	9.8%	9.2%	8.8%	7.0%	33.9%	229.3%	-9.3%

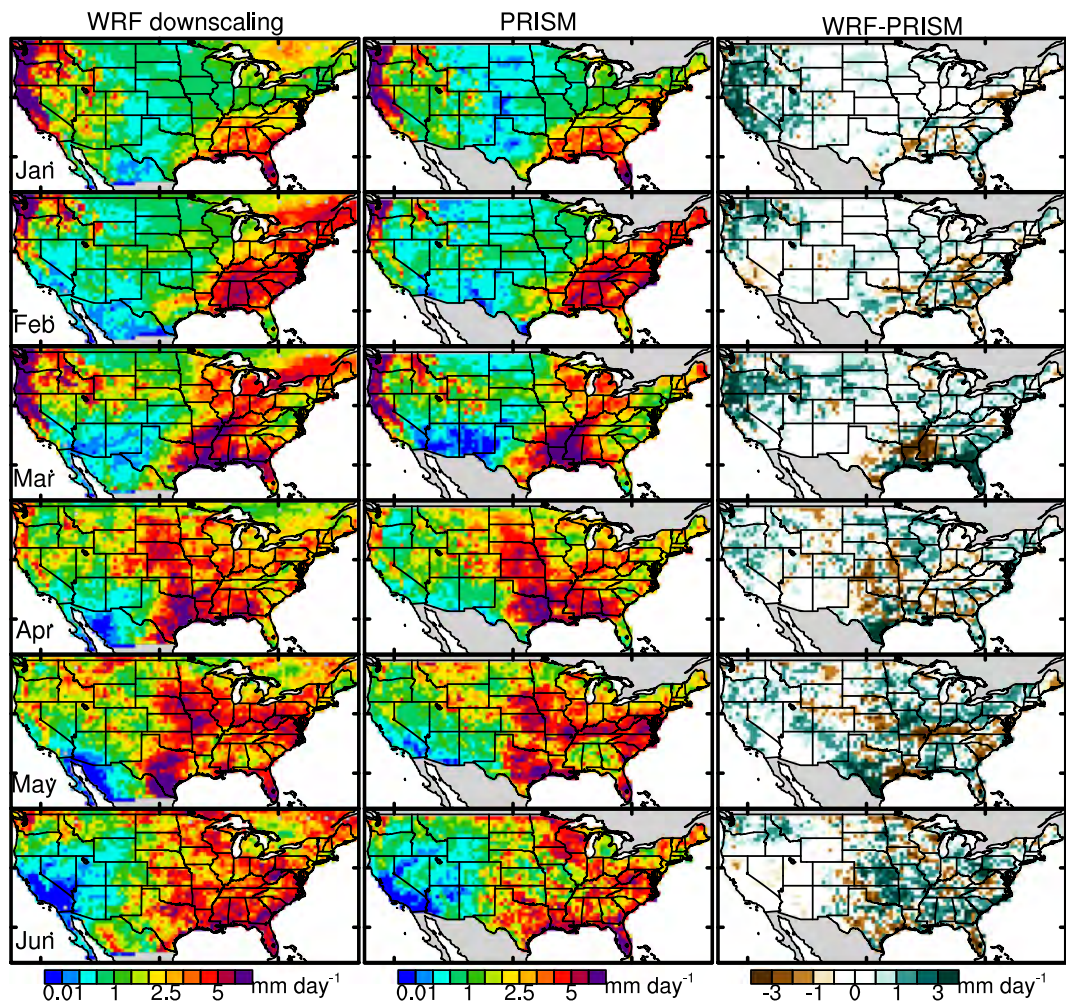


Figure 6. Monthly mean precipitation (in mm/day) (left) downscaled by WRF, (middle) from the PRISM data, and (right) WRF bias (WRF-PRISM) for months (top to bottom) January through June.

2.4.2. Total Carbon Column Observing Network (TCCON) and National Oceanic and Atmospheric Administration Aircraft Observations

We use surface-based TCCON retrievals of XCO₂ for validation of the simulated CO₂ concentrations. The precision and systematic errors in TCCON measurements relative to satellite observations are well understood (e.g., Basu et al., 2013; Dils et al., 2014; Miao et al., 2013), and their sensitivity to regional fluxes provides a valuable check on regional dynamics. Four TCCON sites are chosen for evaluation, Park Falls (WI), Lamont (OK), Caltech (Pasadena, CA), and Dryden (Edwards, CA) with the dominant surrounding vegetation as mixed forest, grass, and shrub, respectively (see their locations in Figure 1). Caltech, located in the Los Angeles basin, is to the southwest of Dryden. Caltech is too close to Dryden over the CONUS domain that the labeling is a problem, thus is omitted in Figure 1.

At two of the TCCON sites, Park Falls (WI) and Lamont (OK), the Global Greenhouse Gas Reference Network's aircraft program (<https://www.esrl.noaa.gov/gmd/ccgg/aircraft/>) has been collecting CO₂ data in vertical profiles up to ~5 km above ground level (AGL). The sampling flights at Park Falls were conducted once every 2 to 3 weeks, while sample flights at Lamont were more often until September 2016 when the sampling discontinued. These data are also used for model evaluation.

2.4.3. ACT-America Data

The ACT-America mission is being conducted to improve the understanding of sources and sinks of CO₂ at regional scale ($\sim 10^6 \text{ km}^2$) and transport of greenhouse gases by weather systems in midlatitudes. During the mission, two aircraft (National Aeronautics and Space Administration, NASA, Wallops C130—Hercules and

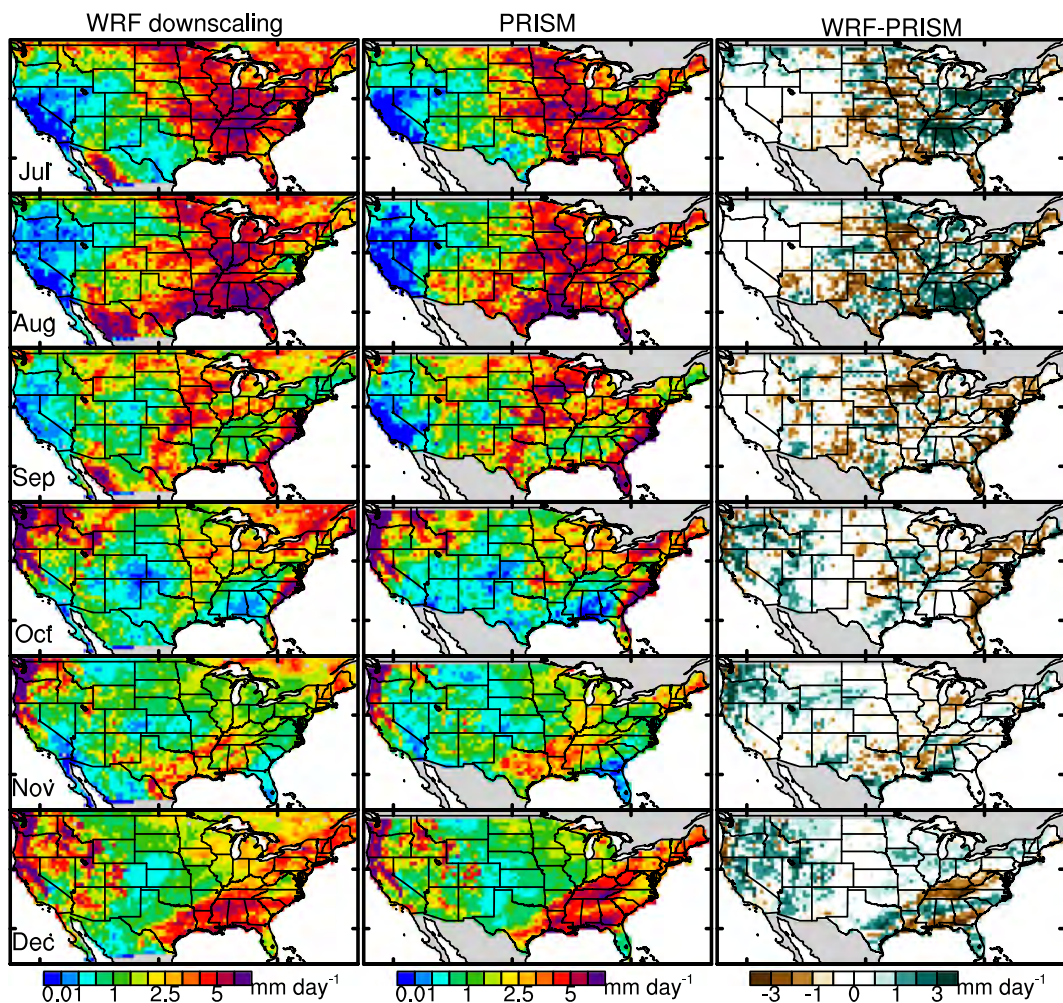


Figure 7. Same as Figure 6 but for months (top to bottom) July through December.

NASA Langley B200—King Air) were deployed to three regions over the eastern half of the CONUS domain during 2016–2018, covering four seasons, to measure meteorological variables and gas species including CO₂ and CH₄ across a variety of weather conditions in both the boundary layer and the free troposphere. Airborne CO₂ and CH₄ were measured using a PICARRO 2401-m analyzer calibrated with gas standards traceable to the World Meteorological Organization scale (CO₂: X2007; CH₄: X2004A) (H. W. Chen et al., 2019). The 2016 ACT-America summer flight campaign data (Digangi et al., 2018) are used to evaluate the CO₂ simulation with the updated WRF-VPRM.

Table 5

Evaluation Statistics for the Simulated Monthly Mean Precipitation Against the PRISM Data in Each Month

Month	1	2	3	4	5	6	7	8	9	10	11	12
Mean obs (mm/day)	1.8	1.8	2.5	2.6	2.6	2.2	2.6	2.9	2.4	2.1	1.6	2.3
Mean sim (mm/day)	2.2	2.0	3.1	2.8	3.0	2.5	2.7	3.0	2.0	2.2	1.8	2.7
r	0.91	0.90	0.80	0.75	0.56	0.72	0.73	0.73	0.77	0.87	0.86	0.79
MB (mm/day)	0.4	0.3	0.6	0.2	0.4	0.3	0.1	0.1	-0.4	0.0	0.2	0.3
MAGE (mm/day)	0.7	0.6	1.1	0.9	1.2	1.0	1.1	1.3	0.9	0.9	0.7	0.9
RMSE (mm/day)	1.2	0.9	2.0	1.3	1.9	1.4	1.6	1.9	1.4	1.4	1.1	1.4
NMB (fraction)	23.5%	14.1%	23.3%	7.5%	14%	13.3%	4.3%	2.2%	-15.6%	1%	13.9%	14.1%

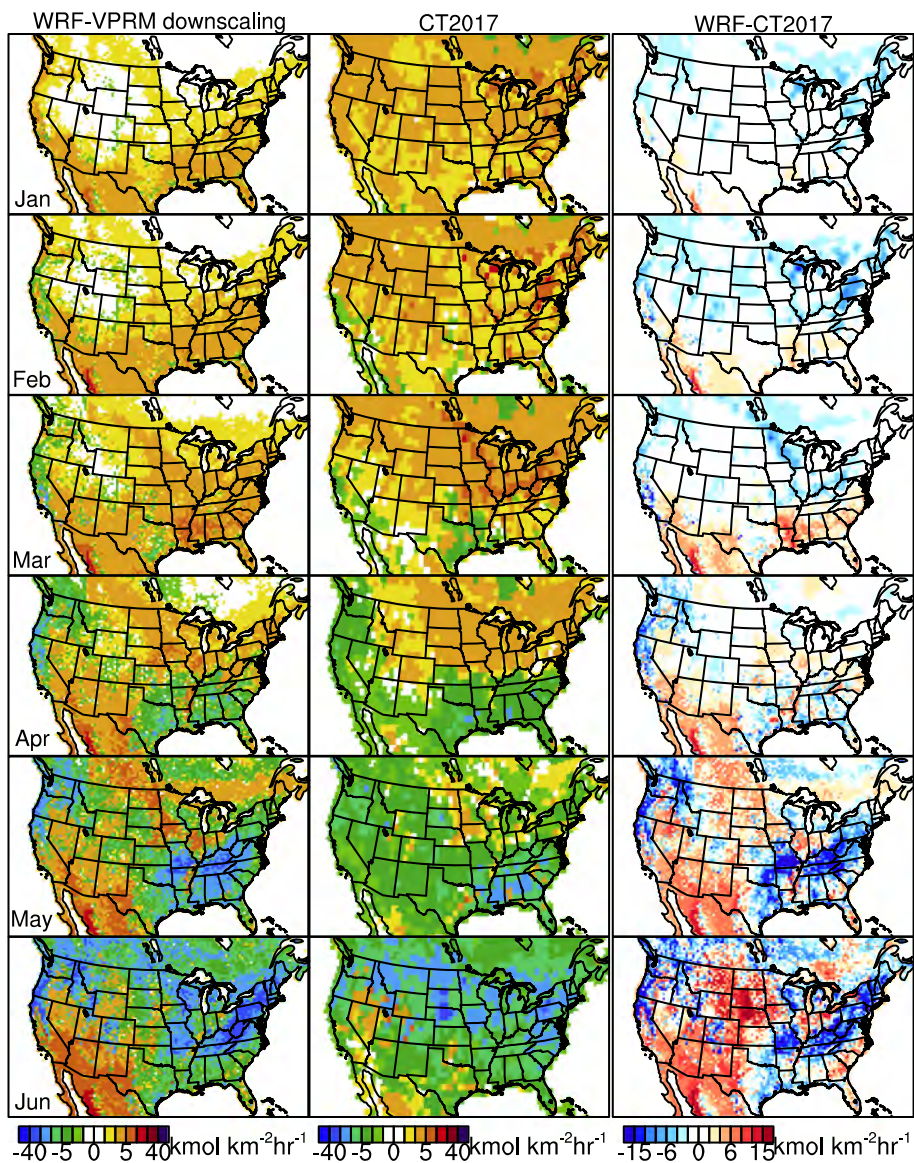


Figure 8. Monthly mean biogenic CO₂ fluxes (in $\text{kmol} \cdot \text{km}^{-2} \cdot \text{hr}^{-1}$) (left) downscaled by WRF-VPRM, (middle) from the CT2017 posterior fluxes, and (right) their difference for months (top to bottom) January through June.

3. Results

3.1. Meteorological Evaluations

The WRF-VPRM downscaling simulation is first evaluated in terms of the surface meteorological fields. The simulated monthly mean temperature at 2 m AGL (T₂) is evaluated using the Parameter-elevation Regressions on Independent Slopes Model (PRISM) data (Daly et al., 1994) in Figures 2 and 3. Note that PRISM produces monthly data on a regular grid over CONUS at a 4-km grid spacing based on point measurements and a digital elevation model (Prat & Nelson, 2015). The WRF-VPRM simulates monthly variations of T₂ and its spatial distributions each month, with correlation coefficients higher than 0.95 (Table 3). The simulation underestimates T₂ over the eastern and western United States and slightly overestimates over central United States, and the errors are much smaller in summer months, with a mean bias of $\sim -0.5^\circ\text{C}$ between May and August (Table 3). The root-mean-square errors range from 1.2°C in May to 2.76°C in February, better than the range of $2.3\text{--}4.0^\circ\text{C}$ of a previous WRF downscaling simulation at a 50-km grid spacing without spectral nudging (Mearns et al., 2012). The largest mean bias of

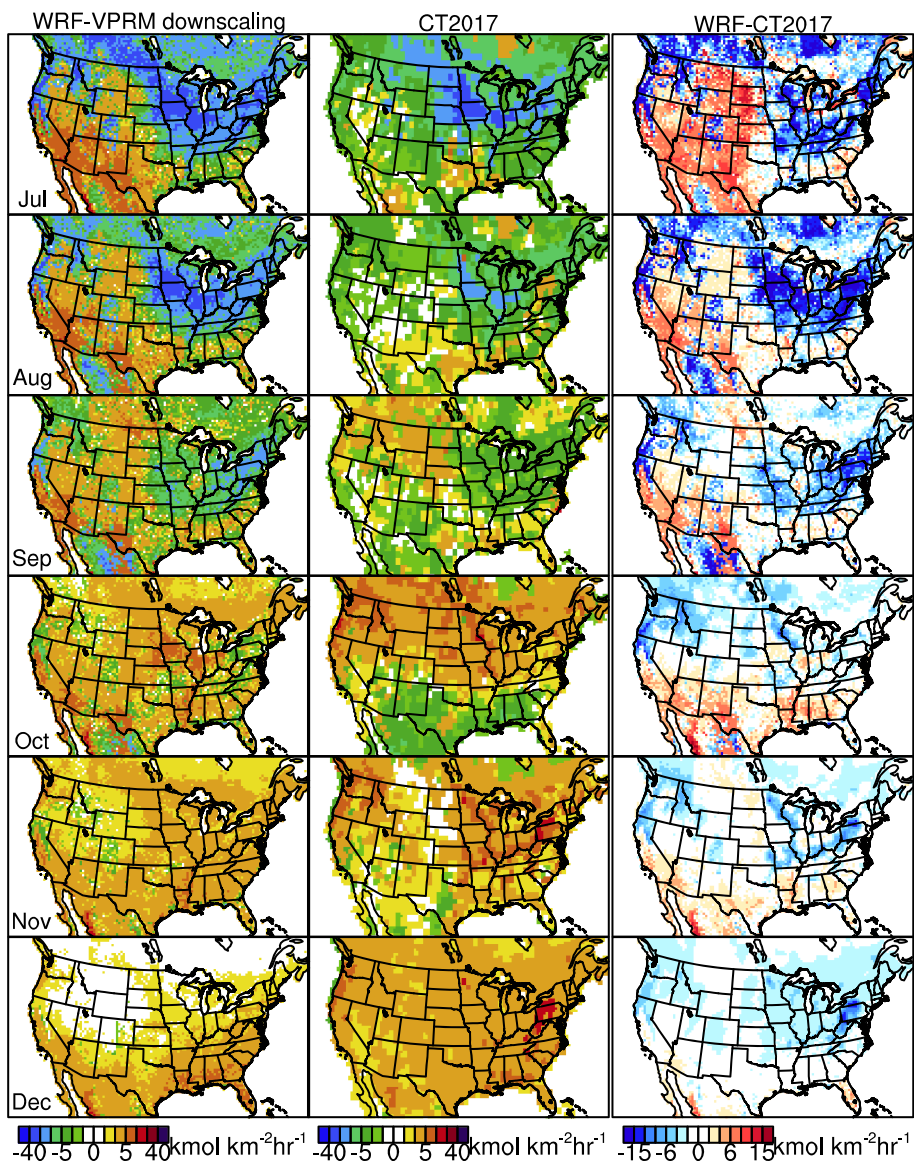


Figure 9. Same as Figure 8 but for months (top to bottom) July through December.

-2.37°C occurs in February in our simulation, with the cold bias most prominent in northern United States and over the Rockies, which may be related to model uncertainties associate with snow cover and its albedo (F. M. Zhang & Pu, 2019). In warm months (from May to August), the downscaling simulation exhibits a warm bias in the central Great Plains with cold biases toward both coasts, consistent with Mearns et al. (2012).

Downscaled monthly mean dewpoint (T_d) at 2 m AGL is also evaluated using the PRISM data in Figures 4 and 5. The spatial correlation coefficients between simulated and PRISM T_d are higher than 0.94 in each month. The overall positive biases of T_d range from 0.56°C in December to 1.79°C in October (Table 4).

Accurate downscaling of precipitation is a more stringent metric for regional dynamic downscaling (Hu, Xue, et al., 2018; X. Sun et al., 2016; Wang & Kotamarthi, 2013). Downscaled monthly mean precipitation rates are compared with the PRISM precipitation data in Figures 6 and 7. The spatial correlation coefficients between the simulation and PRISM range from 0.56 to 0.91 in each month (Table 5). In the cold season, particularly in December to February, precipitation mostly occurs in southeastern United States and the coastal regions of northwestern United States. The simulation exhibits higher correlation coefficients (>0.8) than the rest of the year, due to stronger synoptic-scale forcing in the winter. Starting from April, precipitation

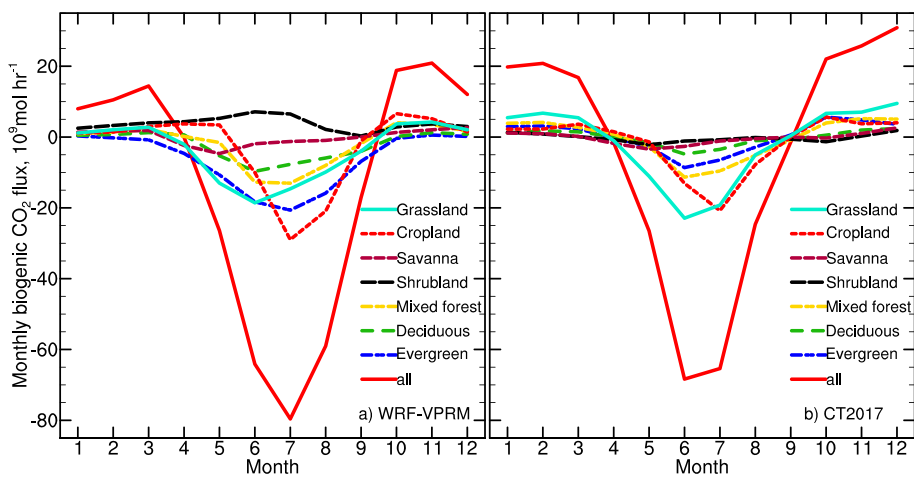


Figure 10. Time series of monthly mean biogenic CO_2 fluxes over the CONUS domain as well as each individual land category shown in Figure 1f, (a) downscaled by WRF-VPRM and (b) from the CT2017 posterior fluxes.

over the Great Plains increases due to the onset of warm-season convection in the region. In June, convection over the Great Plains tapers off as the monsoon ridge sets in. July–September is a challenging period for precipitation downscaling over the Great Plains due to mesoscale vertical circulations, eastward propagating convection, and large-scale moisture advection (Dai et al., 1999; Findell et al., 2011; Hu, Xue, et al., 2018; Liang et al., 2006; Martynov et al., 2013; Qiao & Liang, 2015; Schumacher et al., 2013). Still, the downscaling correctly reproduces the spatial distributions of precipitation during this period in the region and the whole CONUS, though with lower correlation coefficients than the cold season. The downscaling simulation generally overpredicts monthly precipitation except in September (Table 5), which is partially explained by model uncertainties associated with cumulus schemes (Hu, Xue, et al., 2018). The overall wet bias may be partially responsible for the cold biases seen in Figures 2 and 3. Given the above evaluation results, we believe the downscaled meteorological fields, in particular, the low-level fields, are sufficiently accurate to drive the online coupled VPRM model for CO_2 simulation.

3.2. Comparison of Biogenic CO_2 Fluxes Simulated by WRF-VPRM and the CT2017 Posterior Fluxes

Monthly mean biogenic CO_2 fluxes downscaled by WRF-VPRM and the CT2017 posterior fluxes (<ftp://aftp.cmdl.noaa.gov/products/carbontracker/co2/CT2017/fluxes/three-hourly>) are compared in Figures 8 and 9. While both WRF-VPRM and CT2017 give similar spatial distributions of CO_2 fluxes (in terms of source versus sink) and monthly variations with a CO_2 sink in summer (particularly over eastern United States) and CO_2 source in winter, there are qualitative and quantitative differences. In WRF-VPRM, onset of the growing season starts earlier than CT2017 in the Pacific Northwest where evergreen forests dominate, and the growing season in the region extends further into the fall. The mean fluxes over the evergreen forests in summer simulated by WRF-VPRM are more than twice of those given by CT2017 (Figure 10). MODIS-derived EVI starts to increase over the southeast United States in April (figure not shown), indicating starts of the growing season. As a result, the EVI-based VPRM simulates enhanced GEE, thus CO_2 sink, over these regions, consistent with CT2017 (Figure 8). In May, EVI over the southeast United States and West Coast becomes more enhanced and consequently WRF-VPRM simulates prominent CO_2 sink over these regions. In contrast CT2017 simulates moderate CO_2 sink over these regions in this month. VPRM-simulated onset time of prominent GEE (Figure 8) appears to agree with that indicated by Sun-induced fluorescence (SIF) data (Figure 11). Note that SIF is a direct indicator of photosynthetic activity (Krause & Weis, 1991; Song et al., 2016) and is proportional to GEE (Y. Sun et al., 2018). In July, when corn belt (classified as cropland in VPRM) leaf area nearly reaches a maximum (Neild & Newman, 1987), WRF-VPRM simulates stronger CO_2 sink than CT2017 in the region. Such a difference persists into August (Figures 9 and 10). Between April and September when photosynthesis is active, correlation between GEE simulated by WRF-VPRM and SIF maintains above 0.7 (Table 6). During the rest of the year when photosynthesis subsides and SIF's

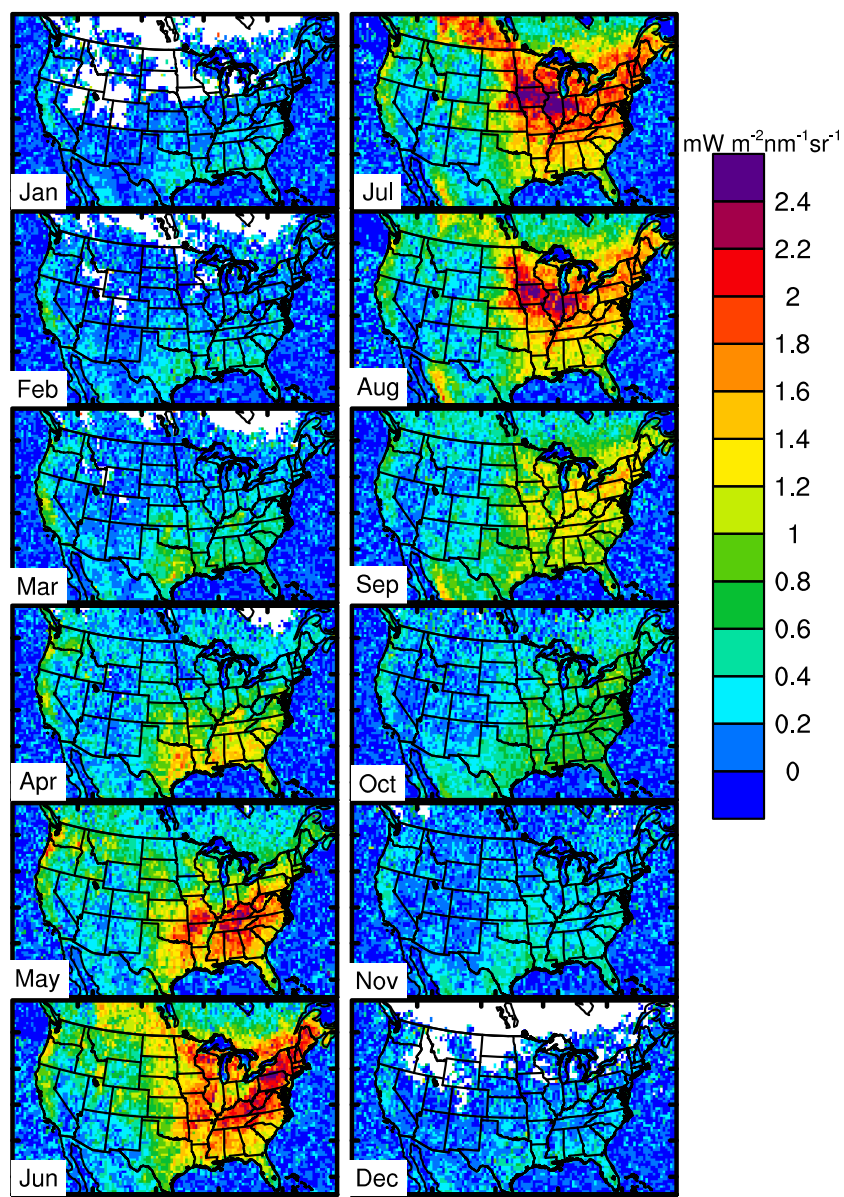


Figure 11. Monthly Sun-induced fluorescence (SIF) in 2016 from the Global Ozone Monitoring Experiment-2 (GOME-2).

spatial variation is quite small, correlation between GEE and SIF decreases below 0.6. In summary, EVI-based WRF-VPRM simulates a CO₂ sink generally consistent with the SIF data in terms of both spatial and temporal variation.

Entering October when photosynthetic activity becomes reduced (Figure 11), both WRF-VPRM and CT2017 simulate CO₂ sources over most area of the continental United States, though CT2017 gives a drawdown

Table 6

Correlation Between Monthly Sun-Induced Fluorescence (SIF, in $mW \cdot m^{-2} \cdot sr^{-1} \cdot nm^{-1}$) and Gross Ecosystem Exchange (GEE, in $kmol \cdot km^{-2} \cdot hr^{-1}$) Simulated by WRF-VPRM Over the CONUS Domain

Month	1	2	3	4	5	6	7	8	9	10	11	12
Mean SIF	0.15	0.16	0.27	0.45	0.71	0.94	0.99	0.86	0.62	0.36	0.20	0.12
Mean GEE	0.52	0.86	1.55	3.79	8.19	13.52	15.69	13.60	8.40	3.11	1.24	0.54
<i>r</i>	0.25	0.39	0.58	0.74	0.78	0.72	0.76	0.77	0.71	0.57	0.49	0.27

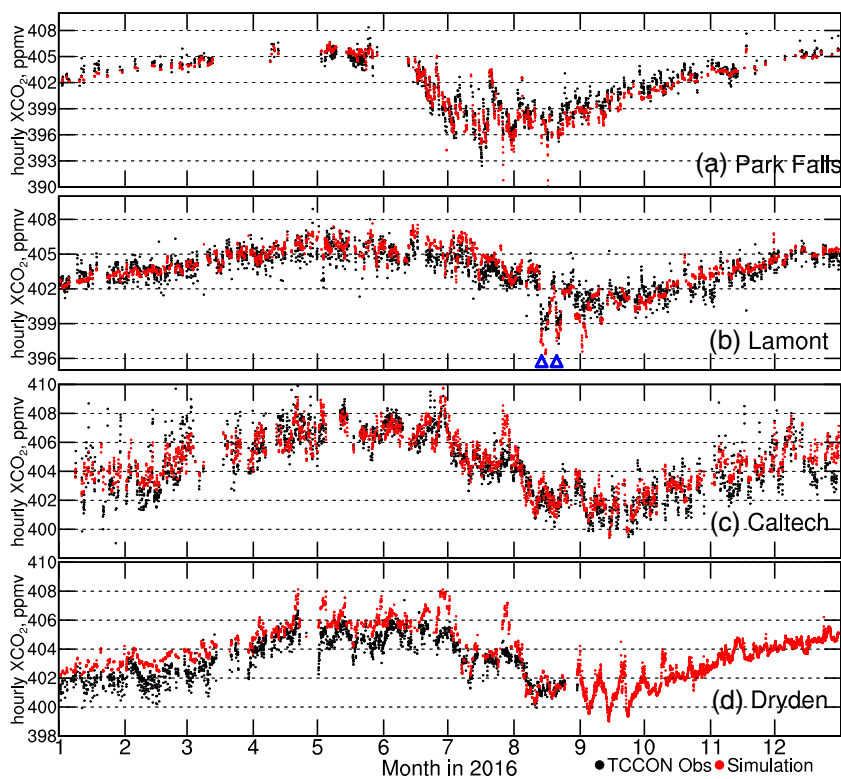


Figure 12. XCO_2 at the TCCON sites in (a) Park Falls, WI, (b) Lamont, OK, (c) Caltech, CA, and (d) Dryden, CA, observed (black) and simulated by WRF-VPRM (red). Two significant drops of XCO_2 at Lamont on 13 and 20 August are marked with triangles.

(negative fluxes) in Southern CONUS in October (Figure 9). In winter, CT2017 appears to have a stronger respiration signal than WRF-VPRM, particularly over the Appalachian Mountains where deciduous forests dominate (Figures 8–10). An enhanced positive CO_2 flux over the Appalachian Mountains in November and December also shows up in the European Centre for Medium-Range Weather Forecasts (ECMWF) Copernicus Atmospheric Monitoring Service (Agusti-Panareda et al., 2014) posterior products (downloaded from <http://apps.ecmwf.int/datasets/data/cams-ghg-inversions/>, figure not shown), similar to CT2017. Over the southwestern United States, where EVI is low throughout the year, GEE is consequently low; meanwhile, ER calculation in VPRM simply depends on temperature following equation 2 and is thus consequently more prominent in summer month. As a result, WRF-VPRM simulates prominent CO_2 sources in the region in summer (Figures 8–10).

3.3. Evaluation of XCO_2 Using Data From Four U.S. TCCON Sites and OCO-2

CO_2 downscaling is first evaluated using the surface-based XCO_2 observation at four TCCON sites: Park Falls (WI), Lamont (OK), Caltech (CA), and Dryden (CA) (Figure 12). Note that XCO_2 is available from Dryden only up to August 2016 (missing data between September 2016 and June 2018). Simulated CO_2 profiles are taken at the TCCON sites and transformed to XCO_2 using weighting by pressure layer thickness:

$$\text{XCO}_2 = \frac{\sum_{l=1}^{l=47} (\text{CO}_2 p)_l}{(p_{\text{bottom}} - p_{\text{top}})} \quad (5)$$

which is equivalent as the method described by Connor et al. (2008) and subsequently used in a few studies (e.g., Bie et al., 2018; Z. C. Zeng

Table 7

Evaluation Statistics for Simulated Column-Averaged CO_2 (XCO_2) Against the TCCON Data at Four Sites

TCCON sites	Park Falls, WI	Lamont, OK	Caltech, CA	Dryden, CA
Mean obs (ppmv)	401.4	403.5	404.4	403.5
Mean sim (ppmv)	401.0	403.7	404.6	404.4
Number of data	1,452	2,461	2,469	1,830
r	0.95	0.88	0.87	0.9
MB (ppmv)	-0.4	0.14	0.2	1.0
MAGE (ppmv)	0.8	0.7	0.8	1.1
RMSE (ppmv)	1.1	1.0	1.1	1.2
NMB (fraction)	-0.1%	0%	0.1%	0.2%

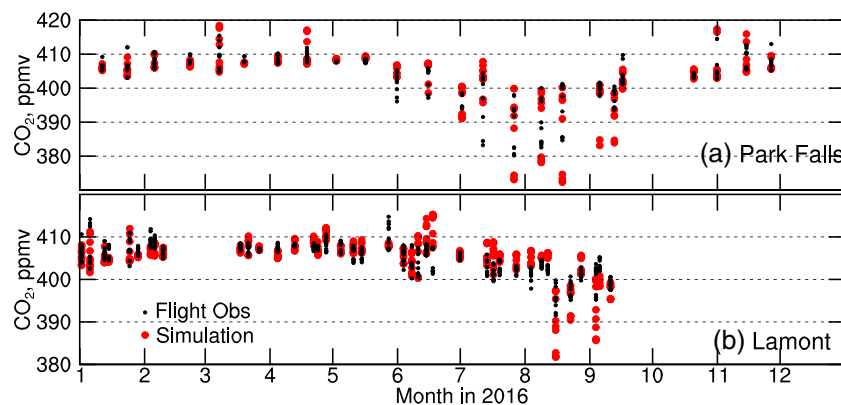


Figure 13. CO_2 at the TCCON sites of (a) Park Falls, WI, and (b) Lamont, OK, collected (black) by the aircraft program of the Global Greenhouse Gas Reference Network (archived at <https://www.esrl.noaa.gov/gmd/ccgg/aircraft/>) and simulated by WRF-VPRM (red). The data points scattered vertically at one time are from the sampled profile on that day.

et al., 2017). Note that simulated XCO_2 was also calculated for a few selected CO_2 profiles using the TCCON retrieval averaging kernel and a priori CO_2 profiles as described in the TCCON documentation. The resulting XCO_2 is very similar to the pressure-weighted XCO_2 , and thus, the simpler pressure-weighted XCO_2 is sufficient for the purpose of evaluating general patterns. Additionally, recent findings indicate that the growth rate in the TCCON prior was too small (D. Wunch, private communication, 2018), which could potentially overwhelm the statistical error induced by the comparison without the prior incorporation. Thus, we report the pressure-weighted average rather than the average incorporating the prior and averaging kernel.

Note that the WRF-VPRM model top pressure (p_{top}) is set to 10 mb, while the TCCON XCO_2 measurement is for the whole atmospheric column. The contribution of CO_2 between 0 and 10 mb to XCO_2 is estimated using simulation outputs from the CarbonTracker model, in which the model top is set at 0 mb. The estimated contribution of CO_2 between 0 and 10 mb is less than 0.1 ppmv over CONUS (figure not shown). Thus, the XCO_2 bias from excluding the contribution from CO_2 between 0 and 10 mb by our WRF-VPRM simulation is negligible.

3.3.1. Comparison With the TCCON Data

WRF-VPRM downscaling captures the monthly variation of XCO_2 at the four TCCON sites quite well (Table 7) with the highest XCO_2 in May and the lowest XCO_2 in the warm season from July to September (Figure 12). The monthly variation of XCO_2 is likely dominated by the monthly variation of NEE and large-scale background CO_2 passed into the domain through the lateral boundary condition derived from the CT2017 data. Park Falls, located in northern Wisconsin and surrounded by mixed forest (Figure 1c), experiences an early green-up as indicated by EVI (figure not shown) and a significant drop of XCO_2 in

Table 8

Evaluation Statistics for Simulated CO_2 Against the Flight Data at Park Falls and Lamont Collected by the Aircraft Program of the Global Greenhouse Gas Reference Network (Archived at <https://www.esrl.noaa.gov/gmd/ccgg/aircraft/>)

Sites	Park falls			Lamont		
	Overall	<1.5 km	>1.5 km	Overall	<1.5 km	>1.5 km
Mean obs (ppmv)	403.2	402.5	403.8	404.9	404.8	404.9
Mean sim (ppmv)	402.9	402.0	403.8	405.1	405.1	405.1
Number of data	226	116	110	469	202	267
r	0.90	0.91	0.90	0.70	0.66	0.79
MB (ppmv)	-0.3	-0.6	0.0	0.2	0.3	0.2
MAGE (ppmv)	2.5	3.5	1.4	2.3	3.3	1.6
RMSE (ppmv)	3.8	5.0	1.9	3.5	4.6	2.3
NMB (fraction)	-0.1%	-0.1%	0	0.1%	0.1%	0

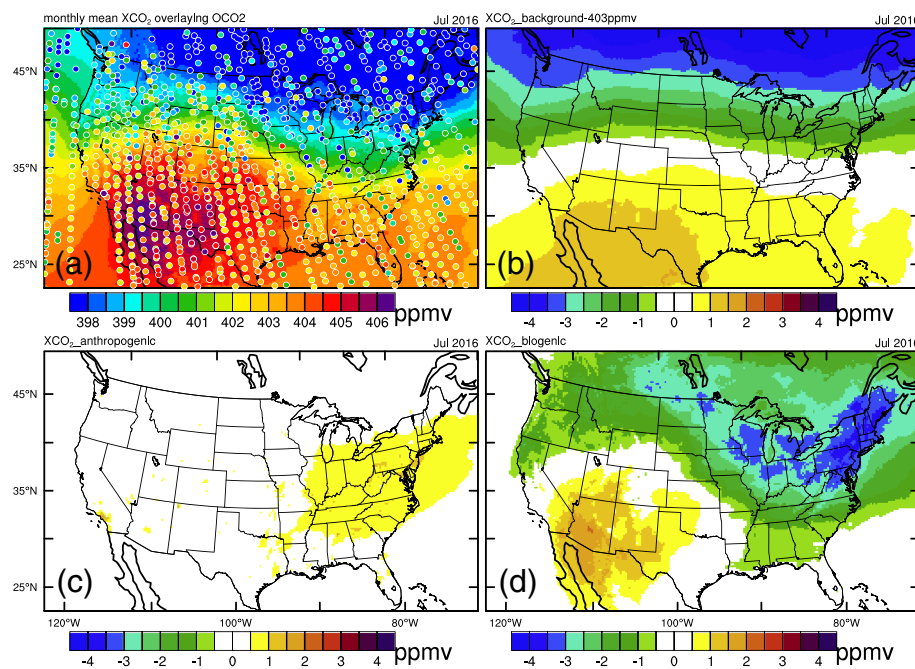


Figure 14. (a) Monthly mean total XCO₂ and individual contribution from (b) background, (c) anthropogenic, and (d) biogenic sources in July 2016. Twenty-second averaged OCO-2 XCO₂ is overlaid in panel (a). Note that a spatially homogenous 403 ppmv is deducted from the background contribution in panel (b).

June, showing an earlier decrease of XCO₂ than Lamont (located in Oklahoma and dominated by grass) and Dryden (located in California and dominated by shrubland). The earlier decrease of XCO₂ at Park Falls is due to significant GEE in June (as will be discussed in next section) and transport of lower-XCO₂ air from the northern domain boundary. The WRF-VPRM simulation underestimates XCO₂ at Park Falls by 0.4 ppmv (Table 7). The CO₂ profiles sampled in the low troposphere by the Global Greenhouse Gas Reference Network's aircraft program (<https://www.esrl.noaa.gov/gmd/ccgg/aircraft/>) also suggest the same seasonality of CO₂ as XCO₂ (Figure 13). Evaluation against the flight CO₂ data also suggests the negative CO₂ biases at Park Falls dominantly come from the atmosphere lower than 1.5 km AGL (Table 8), thus mostly from the atmospheric boundary layer.

Superimposed on the monthly variation, the time series of XCO₂ show some short-term episodic variations, which are caused by synoptic weather systems (i.e., fronts, troughs; Hurwitz et al., 2004) and the diurnal variation of NEE, which results from diurnal variations in PAR and temperature in WRF. WRF-VPRM shows a capability to capture these short-term variations albeit with errors in magnitude. For example, the significant drop of XCO₂ at Lamont on 13 and 20 August (marked in Figure 12b) is due to southward intrusion of two cold fronts (Figure S2 in the supporting information). These episodic events are also sampled by the flights over Lamont (Figure 13) and WRF-VPRM underestimates CO₂ at Lamont in the boundary layer by 5–10 ppmv during these events (profiles not shown). The negative CO₂ biases at Lamont during these two events can be partially traced back to the negative CO₂ biases in the north Center Plains (as far as Park Falls) where the cold front passed by.

The WRF-VPRM captures the monthly variation of XCO₂ at Caltech well (Figure 12c) with a correlation coefficient of 0.87 (Table 7). An accurate anthropogenic emission is critical to reproduce the XCO₂ over Caltech. Our earlier WRF-VPRM simulation with the EDGAR emissions Version 4.2 shows significant overestimation of XCO₂ over Caltech (Hu, Crowell, et al., 2018). Thus, the ODIAC emissions used by this study appear to be more accurate (relative to TCCON) than EDGAR, at least over Los Angeles.

The WRF-VPRM captures the monthly variation of XCO₂ at Dryden but shows systematic overestimation with a mean bias of 1.0 ppmv (Table 7). Evaluation of CT2017 XCO₂ also indicates an overestimation at this site (Hu, Wang, et al., 2019). The overestimation of XCO₂ at Dryden is presumably due to the uncertainties in

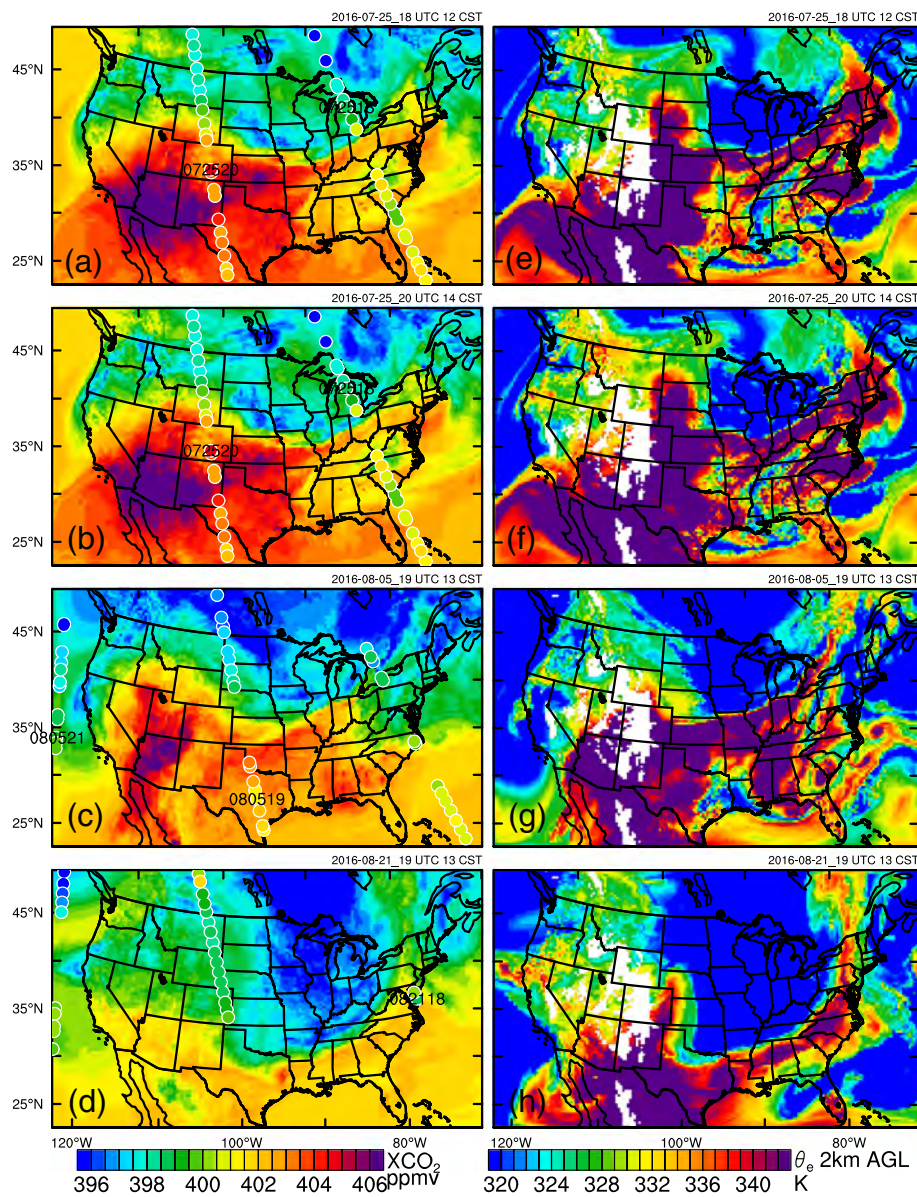


Figure 15. WRF-VPRM simulated spatial distribution of XCO₂ on (a, b) 25 July, (c) 5 August, (d) 21 August 2016, overlaid with the XCO₂ observation from OCO-2 (dots) and (e–h) simulated equivalent potential temperature (θ_e) at 2 km above sea level at the corresponding times. OCO-2 swept eastern United States and Rockies at ~1800 and 2000 UTC on 25 July; thus, simulated XCO₂ at those times is shown in panels (a) and (b).

the parameterization of ER over southwestern United States as mentioned above, as well as the uncertainties in the ODIAC emissions. During two periods (27–28 June and 27–28 July), the WRF-VPRM predicts two spikes of XCO₂ at both Dryden and Caltech and significantly overestimates XCO₂ at the two sites (less so at Caltech). During these periods, low-pressure centers (Hurricane Frank in case of 27 July) developed off the southwest coast (figures not shown). The atmospheric circulation associated with the low-pressure centers transports simulated high-XCO₂ air mass from southwest United States and Mexico (due to overestimated respiration from shrubland) to California, leading to overestimation of XCO₂ at the two sites. Overestimated respiration over southwest United States and Mexico also partially contributes to overestimation of boundary layer CO₂ at Lamont in the presence of southerly transport (see the two significant overestimation cases in June in Figure 13b). More discussions are given in the next section when analyzing individual contributions from different sources.

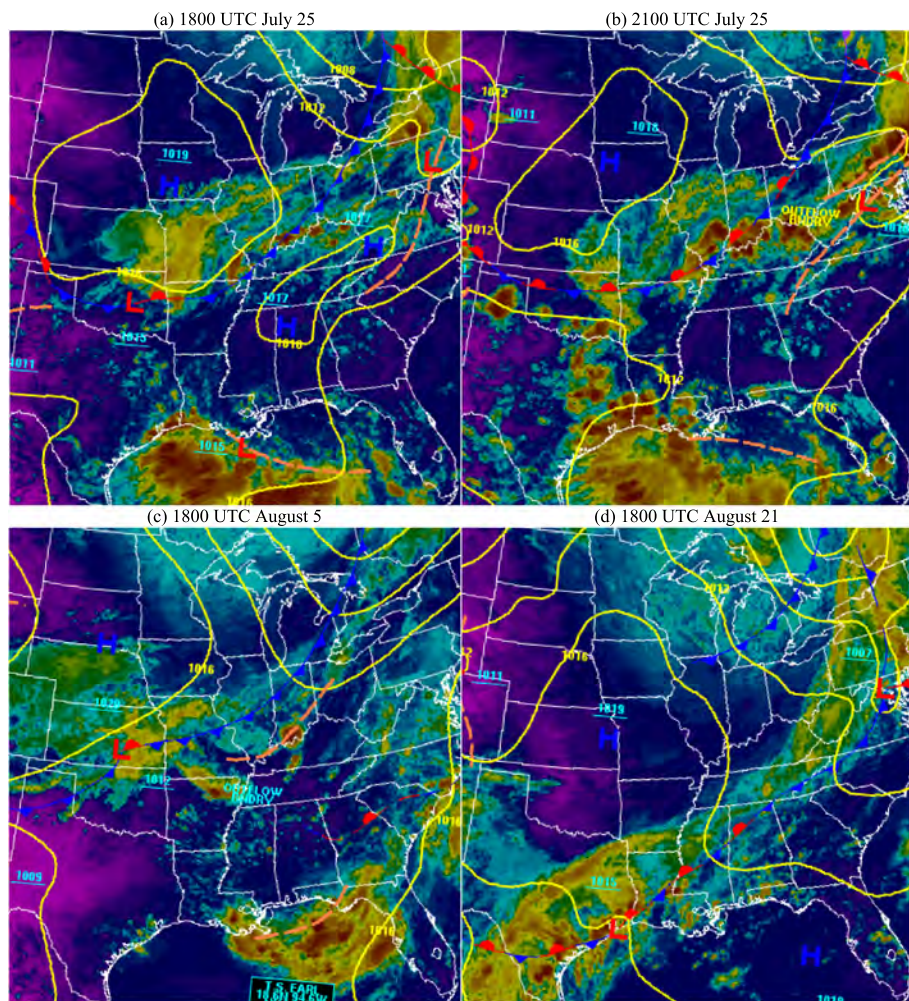


Figure 16. Surface weather analysis overlaid with satellite infrared image at (a) 1800 UTC, (b) 2100 UTC on 25 July, (c) 1800 UTC on 5 August, and (d) 21 August 2016, which were prepared and archived by the Weather Prediction Center of the National Centers for Environmental Prediction (https://www.wpc.ncep.noaa.gov/archives/web_pages/sfc/sfc_archive.php).

3.3.2. Comparison With the OCO-2 Data

Simulated XCO₂ by WRF-VPRM is also compared with OCO-2 XCO₂ observations. Simulated monthly mean XCO₂ at 19 UTC in July 2016 is overlaid with all the OCO-2 XCO₂ observations (ranging from 18 UTC over the eastern United States to 21 UTC over the west coast) on each day in this month in Figure 14a. Even though the simulated XCO₂ displayed is the monthly mean and the OCO-2 XCO₂ observations are instantaneous values, both of them indicate a prominent north to south gradient of XCO₂ in this month, driven by large-scale differences in surface fluxes as well as synoptic forcing. This north to south gradient of XCO₂ over CONUS starts to develop in June and subsides in September (figures not shown), with July and August being most prominent. Different weather systems, particularly fronts, lead to deviation of spatial distribution of XCO₂ on individual days from the monthly mean distribution.

Three frontal cases during the ACT-America 2016 summer campaign (i.e., 25 July and 5 and 21 August) are shown in Figure 15. Weather analysis indicates that arctic air pushed southeastward through a cold front in all these cases and became stationary on 25 July and 21 August (Figure 16). Simulated front locations are illustrated in Figure 15 using the spatial distribution of XCO₂ and equivalent potential temperature (θ_e); the sharp gradient zones of the two fields across the fronts are generally colocated. Since the OCO-2 passed eastern United States at ~18 UTC and Rockies at ~20 UTC, the simulated XCO₂ at these two times on 25 July is shown in Figures 15a and 15b, in which a slight southeastward movement of a frontal system over the

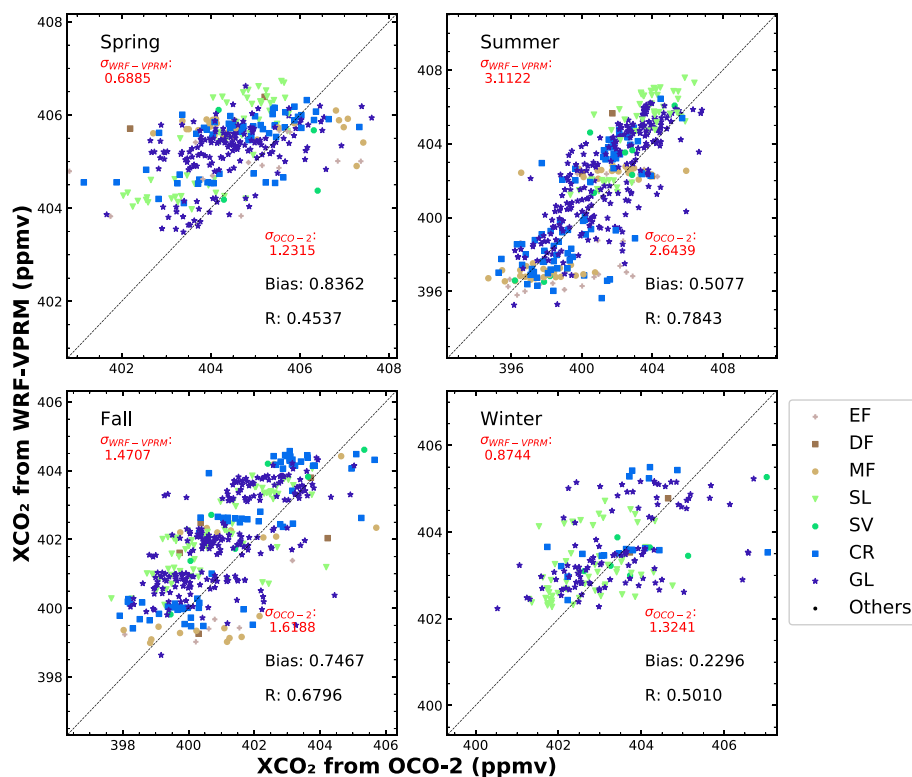


Figure 17. Correlation between XCO₂ from OCO-2 and WRF-VPRM for four seasons in 2016. The data pairs are differentiated into different land categories, including evergreen forest (EF), deciduous forest (DF), mixed forest (MF), shrubland (SL), savannah (SV), cropland (CR), and grassland (GL). The overall standard deviation, bias (in ppmv) and correlation coefficient are included. Note that because of less OCO-2 data at latitudes above 40° N in winter, data pairs are fewer in winter over the land categories that have significant coverages over high latitudes, for example, evergreen forests, deciduous forests and mixed forests.

Midwest during the 2 hr can be noticed as indicated by the cross-front gradient of XCO₂ and θ_e. The simulated frontal movement is consistent with two surface weather analysis during a 3-hr period (Figures 16a and 16b), which indicates that a southeastward moving cold front at 1800 UTC became stationary at 2100 UTC on 25 July. In all three cases, the WRF-VPRM simulation captures the cross-front

Table 9

Standard Deviation of XCO₂ From WRF-VPRM (σ_W) and OCO-2 (σ_O), Bias, T Score With 90% Confidence, and Correlation Coefficient for Each Land Cover Type for 4 Seasons in 2016

	Samples	σ_W	σ_O	Bias	T score (P)	R		Samples	σ_W	σ_O	Bias	T score (P)	R
	Spring						Summer						
Evergreen	15	0.6	1.7	0.3	0.72 (0.48)	0.43		25	2.6	2.6	-1.5	-3.03 (0.01)	0.58
Deciduous	2	0.3	1.5	2.3	2.01 (0.29)	1.00		3	1.6	1.6	1.5	0.90 (0.46)	-0.11
Mixed	28	0.2	1.3	0.9	3.38 (0.01)	-0.17		47	2.8	2.7	-0.3	-1.05 (0.30)	0.80
Shrubland	59	0.9	1.0	1.1	14.16 (10 ⁻²⁰)	0.81		53	2.0	1.7	1.6	9.63 (10 ⁻¹³)	0.80
Savannah	4	0.8	1.0	-0.2	-0.26 (0.81)	-0.12		9	3.5	2.7	0.5	0.93 (0.38)	0.90
Cropland	54	0.6	1.2	0.8	5.52 (10 ⁻⁶)	0.59		76	2.9	2.3	0.2	1.10 (0.28)	0.74
Grassland	164	0.6	1.0	0.8	10.84 (10 ⁻²¹)	0.46		243	2.6	2.4	0.7	6.56 (10 ⁻¹⁰)	0.78
	Fall						Winter						
Evergreen	7	0.8	1.4	-1.2	-2.80 (0.03)	0.70		0	—	—	—	—	—
Deciduous	5	1.5	1.9	0.2	0.20 (0.85)	0.54		2	0.6	0.5	-0.1	-0.18 (0.89)	1.00
Mixed	21	1.8	1.8	-0.2	-0.62 (0.54)	0.60		0	—	—	—	—	—
Shrubland	68	1.1	1.4	1.2	9.56 (10 ⁻¹⁴)	0.73		57	0.7	0.9	0.4	3.77 (0.01)	0.39
Savannah	7	1.6	1.9	0.7	2.00 (0.09)	0.88		7	0.7	1.4	-0.5	-1.57 (1.17)	0.84
Cropland	70	1.9	1.9	0.7	5.10 (10 ⁻⁶)	0.84		19	0.9	1.2	0.3	1.26 (0.22)	0.40
Grassland	224	1.3	1.4	0.8	10.89 (10 ⁻²²)	0.66		103	0.9	1.3	0.2	1.48 (0.14)	0.52

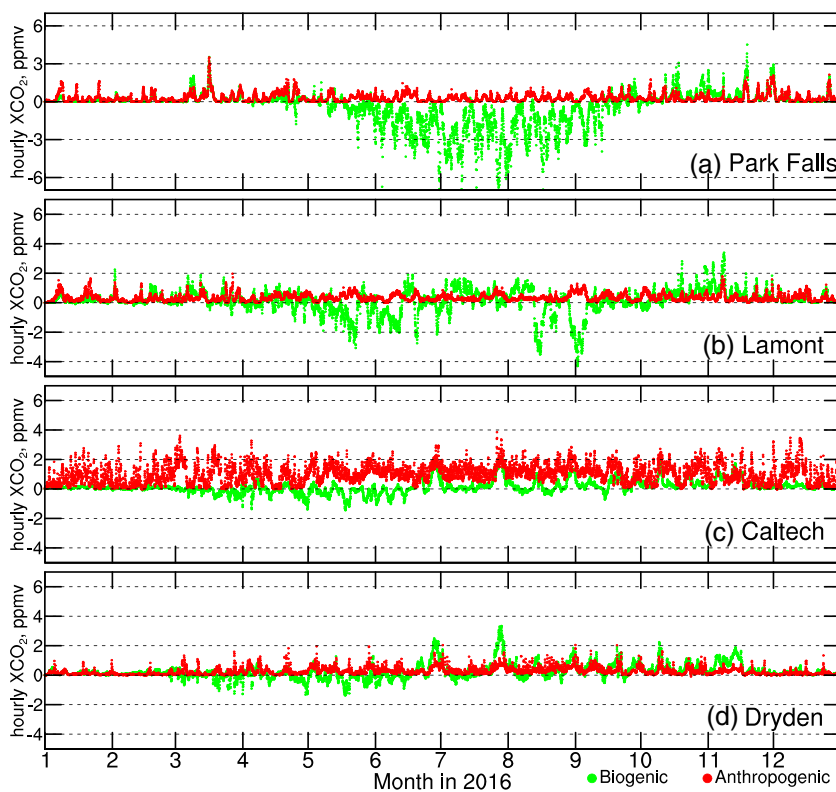


Figure 18. Individual contribution to XCO₂ from anthropogenic, and biogenic sources at TCCON sites (a) Park Falls, WI, (b) Lamont, OK, (c) Caltech, CA, and (d) Dryden, CA.

gradient of XCO₂, that is, lower XCO₂ behind the fronts and higher XCO₂ ahead of the fronts, consistent with OCO-2 data (Figure 15) and Penn State's in situ analyses of summer 2016 cold fronts (Pal et al., 2020).

Statistics of time-matched XCO₂ data pairs between WRF-VPRM and OCO-2 are calculated for each season in 2016 (Figure 17) over seven land cover types over the U.S. domain: evergreen forest, deciduous forest, mixed forest, shrubland, savannah, cropland, grassland (see the spatial distribution of land covers in Figure 1f). In Figure 17, each marker stands for data aggregated in a $1^{\circ} \times 1^{\circ}$ grid box. Outliers falling outside of 3 standard deviations are removed, which might be due to errors in the OCO-2 data, for example, contaminated by clouds. Overall, WRF-VPRM performs better in summer ($R = 0.78$) than other seasons ($R < 0.7$), even though both the observations and the simulations have larger scatter. Generally speaking, WRF-VPRM underestimates XCO₂ over higher-latitude forests and overestimates XCO₂ over shrublands, croplands, and grasslands, though these features are not always statistically significant (Table 9). For example, the model overestimates XCO₂ all year long over shrubland ($P < 0.001$), which dominates in the southwestern United States where temperature is high (Table 9). The positive bias of XCO₂ over shrubland may be due to model error associated with the current simple parameterization of respiration (equation 2), which linearly depends on air temperature and ignores dependency on leaf mass. Recent studies suggest an exponential dependence of terrestrial respiration on air temperature and partial contribution from GPP as well (Migliavacca et al., 2011). Leaf respiration, an important portion of total terrestrial respiration, is proportional to total leaf biomass (Braendholt et al., 2018; Tang et al., 2008). However, such a dependency is not considered in VPRM. The model bias in the area could be also attributed to a lack of flux towers in this region that can be used to properly calibrate VPRM and/or a poor representation of moisture availability in arid conditions.

3.4. Contribution to XCO₂ From Anthropogenic, Biogenic, and Oceanic Sources

Given the satisfactory performance of simulated XCO₂ as demonstrated in the evaluations above, we use the WRF-VPRM outputs to examine the individual contribution to XCO₂ from anthropogenic, biogenic, and oceanic sources. The contribution from oceanic sources within the modeling domain is a few tens of ppbv

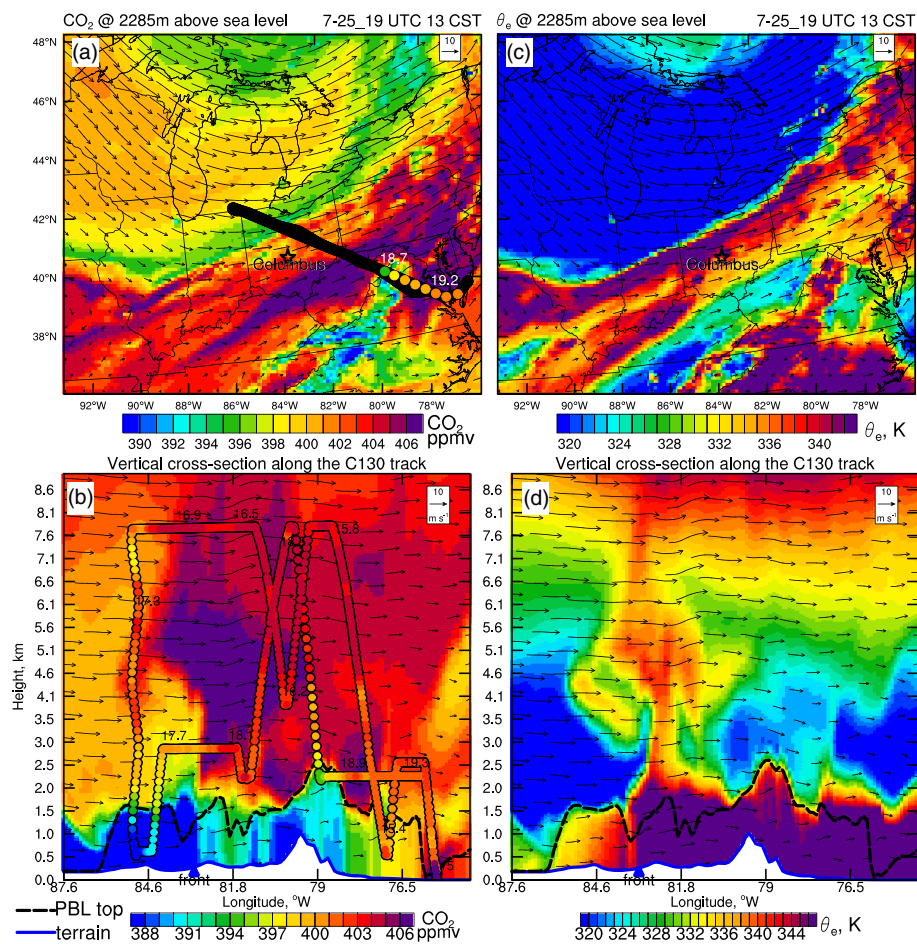


Figure 19. (a, c) Horizontal (at 2,285 m above sea level) and (b, d) vertical cross sections of CO_2 and equivalent potential temperature (θ_e) at 1900 UTC on 25 July simulated by WRF-VPRM, overlaid with C130 aircraft CO_2 data. Note that the flight path and CO_2 data at 2,285 m above sea level is marked in panel a. The black segment of the flight path means the path is not at 2,285 m. Each flight took a few hours, the UTC time is marked along the flight path, while the cross section of simulated CO_2 is an instantaneous snapshot. C130 flew over the Appalachian Mountains at ~1900 UTC. The simulated front location is marked with a blue triangle in panels (b) and (d).

(figure not shown), while the contributions from anthropogenic and biogenic sources are on the order of a few ppmv (Figures 14c and 14d). Background CO_2 (transport from the lateral boundary conditions extracted from CT2017) provides a north-south gradient of XCO_2 (Figure 14b). Superimposed on the background CO_2 , biogenic CO_2 plays the most significant role in shaping the spatial distribution of XCO_2 over the CONUS domain during the peak growing season. Biogenic fluxes dominate anthropogenic sources to modulate XCO_2 over most of CONUS except a few metropolitan areas such as Los Angeles in growing season starting from May to September (figure not shown). Significant biogenic CO_2 uptake fluxes start in May, depleting local XCO_2 by 1–2 ppmv over southeast United States (figure not shown), and become more prominent in July, decreasing XCO_2 by 3–4 ppmv over the corn belt and northeast United States (Figure 14d); meanwhile, biogenic CO_2 fluxes increase XCO_2 over southwestern United States in summer.

Even though the WRF-VPRM anthropogenic emissions (derived from ODIAC) include monthly variation, such a variation is moderate, and the contribution of anthropogenic emissions to XCO_2 has only a weak seasonal variation (Figure 18). In contrast, the biogenic contribution shows a prominent seasonal variation. Particularly at Park Falls, in warm months, VPRM simulates a negative biogenic contribution, indicating vigorous biogenic fluxes. At Lamont, there are three prominent spikes of biogenic contributions on 13 and 20 August, and at the beginning of September, which are due to the southward front penetration into Oklahoma (see National Oceanic and Atmospheric Administration frontal analysis in the supporting

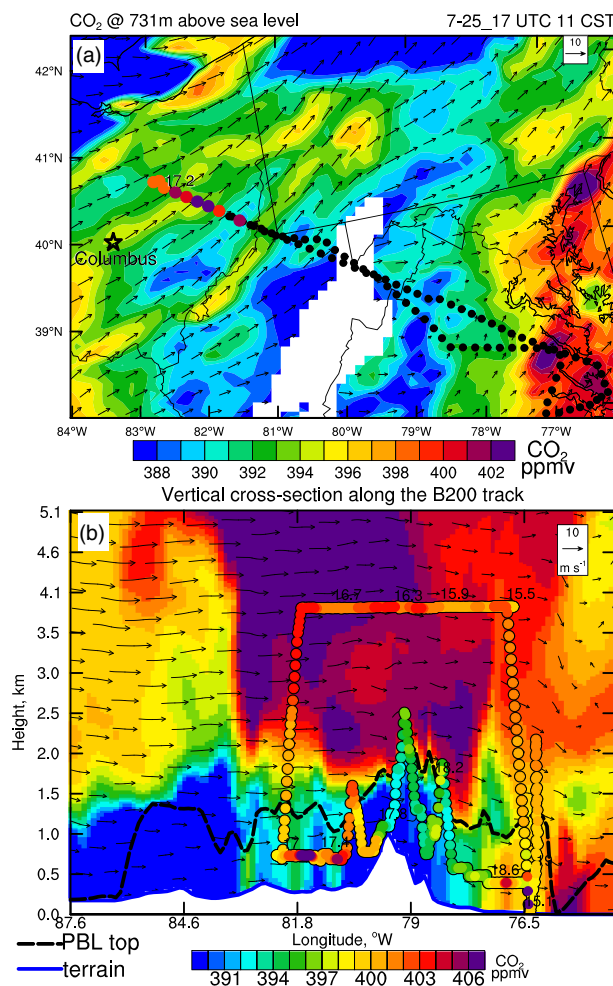


Figure 20. (a) Horizontal (at 731 m above sea level) and (b) vertical cross sections of CO₂ at 1700 UTC on 25 July simulated by WRF-VPRM, overlaid with B200 aircraft data. Note that CO₂ data at 731 m above sea level is marked in color shading and the flight path at other altitudes is marked with black dots in panel (a).

are critical to simulate CO₂ over the United States. For the 1-year continuous CO₂ downscaling simulation conducted in study, its sustained capability to reproduce fronts throughout the year is a concern and is examined using the data collected by the NASA Wallops C130 and Langley B200 deployed by ACT-America from 11 July to 28 August 2016 over three regions: Northeast, Midwest, and Southeast coastal regions. The WRF-VPRM downscaling captures the location of major frontal events throughout the entire downscaling simulation (figures not shown) and captures the cross-front gradients of CO₂. Three frontal cases from the campaign (25 July and 5 and 21 August, one for each region) are selected to illustrate the performance of WRF-VPRM in terms of capturing the front and CO₂ gradient across the fronts, as well as vertical gradients across the boundary layer top. Note that on 5 August the aircraft collected coincident observations with OCO-2, and the flights crossed a sloping frontal boundary in the upper troposphere.

3.5.1. Case 1, 25 July Over the Northeast Region

On 25 July, the C130 aircraft took off from the NASA Wallops flight center at ~15 UTC, first ascended in a shallow boundary layer (~500 m) with rich CO₂ (>406 ppmv) (Figure 19b). WRF-VPRM simulated boundary layer CO₂ shows a prominent variation above 400 ppmv east of the Appalachian Mountains even though the boundary layer heights are homogeneously ~500 m in the region at the time. Thus, the observed high CO₂ in the boundary layer by the aircraft is likely attributable to the anthropogenic emissions emanated from the urban corridor along the interstate 95 highway (Figure 1b) and confined in the shallow morning

information). These fronts bring in low XCO₂ air in which CO₂ is depleted due to significant NEE over the corn belt in the north (figure not shown).

At Dryden, VPRM simulates more prominent positive biogenic contributions in warm months than negative biogenic contributions, indicating the contributions from terrestrial respiration outweigh those from photosynthesis. As discussed above, the current VPRM model parameterization likely artificially overestimates respiration over southwest United States where shrubland dominates, particularly in warm months when temperature is high. Meanwhile, EVI in the southwestern United States is relatively low (Figure 1a), thus GEE is low at Dryden. More vigorous respiration and low GEE collectively lead to positive biogenic contribution to XCO₂ at Dryden in the warm season. At Caltech, anthropogenic contributions dominate biogenic contributions during most of 2016 and the anthropogenic contribution to XCO₂ is much higher than the other three TCCON sites due to the anthropogenic emissions from the Los Angeles metropolitan area (Figure 1b). During the two periods 27–28 June and 27–28 July, when WRF-VPRM predicts two spikes of XCO₂ (Figure 12), biogenic contribution also shows two spikes at both Dryden and Caltech (Figure 18), which further corroborate our previous diagnosis: On these days, the atmospheric circulations associated with low-pressure centers off the southwest coast transport artificially high XCO₂ air mass from shrubland to California, which leads to overestimation of XCO₂ at the two California TCCON sites. These overestimations further demonstrate that the current biogenic fluxes estimated by VPRM over shrubland warrant further improvement.

3.5. Three Case Studies During the ACT-America 2016 Summer Campaign

Strength and frequency of cold fronts associated with midlatitude baroclinic cyclones play important roles to modulating the abundance of trace gases over the United States (Hu, Xue, et al., 2019; Leibensperger et al., 2008). Cold fronts often push polluted continental air out over the Atlantic and replace it with cleaner air, thus improving air quality in the United States (Leibensperger et al., 2008). Similarly, given the meridional gradients of CO₂, particularly in warm season (Figure 14b), as well as impacts of fronts on terrestrial fluxes, correctly reproducing these fronts

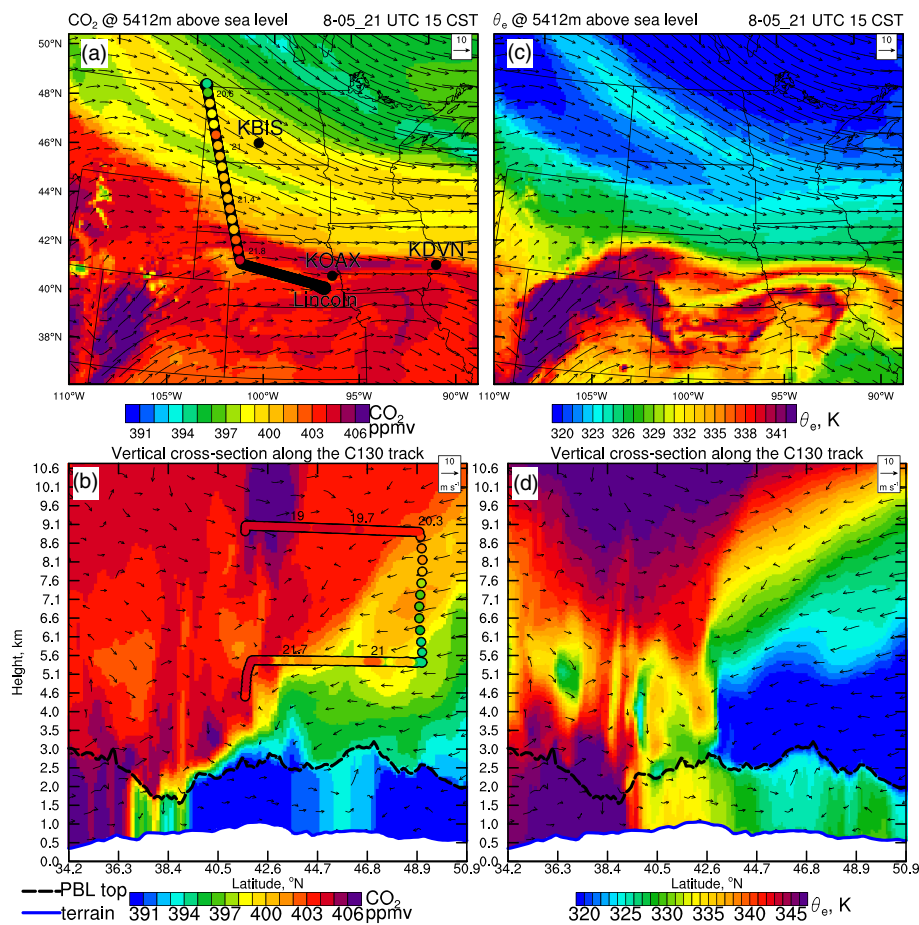


Figure 21. (a, c) Horizontal (at $\sim 5,412$ m above sea level) and (b, d) vertical cross sections of CO₂ and equivalent potential temperature (θ_e) through the OCO-2 underpass (see Figure 15c for the OCO-2 pass) at 2100 UTC on 5 August simulated by WRF-VPRM, overlaid with C130 aircraft CO₂ data. Note that the flight path and CO₂ data at $\sim 5,412$ m above sea level is marked in panel (a). The UTC time is marked along the flight path. In panel (b), the C130 data not on the OCO-2 pass are not shown.

boundary layer. Later on, C130 crossed a few states in the northeast United States and reached Michigan. In the far northwest end of the flight path, C130 crossed a southeastward moving cold front as illustrated by the strong contrast of equivalent potential temperature (θ_e) and wind field across the front (Figure 19c). Both observation and simulation show lower CO₂ behind the front and higher CO₂ ahead of the front. Note that simulated and observed XCO₂ also show the same spatial gradient across the front (Figure 15a,b). On the return path between 18.5 and 18.9 UTC, C130 descended below 2,300 m above sea level at 79°W, experiencing decreasing concentration of CO₂ (Figure 19b). The WRF-VPRM simulation captures the vertical gradient of CO₂ and indicates C130 plunged into the boundary layer. Note that the simulated boundary layer top is marked in Figure 19b using black dashed line. Other species measured by C130, for example, ozone (O₃) and carbon monoxide (CO), all indicate C130 plunged into the boundary layer at this time (figure not shown). This location is above the Appalachian Mountains, dominated by deciduous forest. The lower boundary layer CO₂ is likely due to prominent GEE over the deciduous forest (figure not shown). Previous simulation with the default WRF-VPRM configuration showed significant overestimation of boundary layer CO₂ over the Appalachian Mountains and indicates a parametric model error (Hu, Zhang, et al., 2018). Using the parameters calibrated by Hilton et al. (2013), the updated WRF-VPRM successfully alleviated the overestimation issue over the Appalachian Mountains in this study.

On this day, B200 flew nearly in the same cross section as C130, but at a lower altitude than the C130 and sampled more in the atmospheric boundary layer (Figure 20). While both WRF-VPRM simulation and B200 indicate reduced boundary layer CO₂ level above the Appalachian Mountains, the modeled CO₂ is

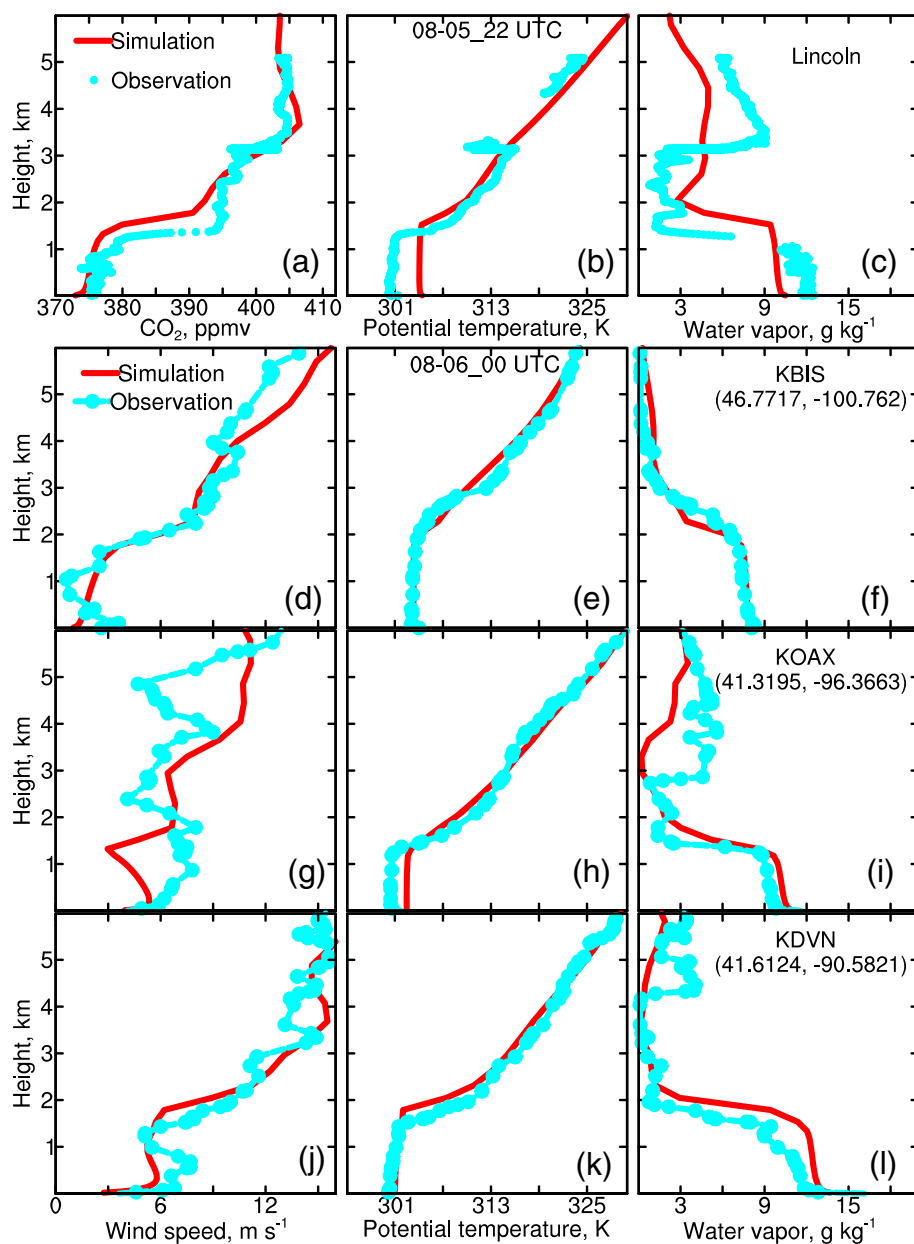


Figure 22. (a–c) Profiles of CO₂, potential temperature (θ), and water vapor mixing ratio simulated at 2200 UTC and observed during the C130 descending time between 2200 and 2240 UTC on 5 August over the Lincoln airport (40.8367°N, 96.7619°W), and profiles of (left to right) wind speed, θ , and water vapor mixing ratio at 0000 UTC on 6 August simulated and observed at sounding sites: (d–f) KBIS, (g–i) KOAX, and (j–l) KDVN, which are marked on Figure 21a.

lower than the measurements in the boundary layer west of the Appalachians. A few CO₂ plumes in Ohio are simulated in the region, which were intercepted by B200, including the one from Columbus (Figure 20a). The simulated plumes are biased low relative to the aircraft observations. Model errors associated with VPRM may also contribute to the CO₂ bias.

3.5.2. Case 2, 5 August Over the Midwest Region

On 5 August, the C130 aircraft flew west and then followed the OCO-2 track on this day (see OCO-2 track in Figure 15c). During the flight, C130 first flew northward at ~9 km above sea level, over an sloping front. On this day surface cold front penetrated southward into Oklahoma (Figure 16c), while the front boundary persisted over South Dakota at ~5 km above sea level (Figure 21c). Since the flight track was mostly ahead of the

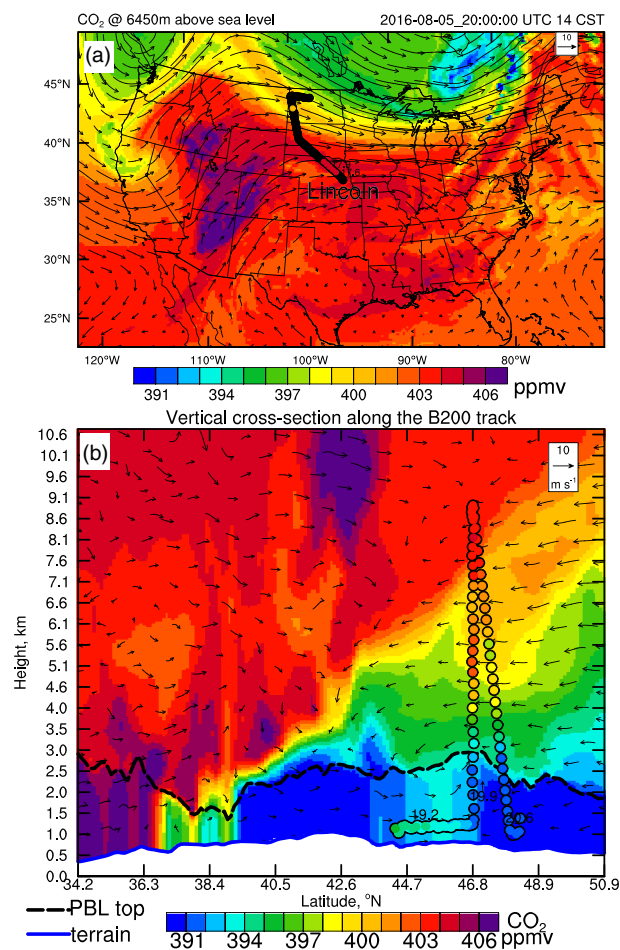


Figure 23. (a) Horizontal (at ~6,450 m above sea level) and (b) vertical cross sections of CO₂ through the OCO-2 underpass (see Figure 15c for the OCO-2 pass) at 2000 UTC on 5 August simulated by WRF-VPRM, overlaid with B200 aircraft data. Note that the flight path and CO₂ data at ~6,450 m above sea level is marked in panel (a). The black segment of the flight path means the path is not at 6,450 m. The UTC time is marked along the flight path. In panel (b), the B200 data not on the OCO-2 pass are not shown.

the front. The vertical gradient of CO₂ is nicely reproduced by the model. The model also captures the near-surface CO₂ plume along the western side of South Dakota and North Dakota (Figure 23b).

The vertical profiles during the B200 taking off at 1700 UTC are also compared. The boundary layer structure is well captured by the model (Figure 24b), but WRF-VPRM underestimates boundary layer CO₂ by ~6 ppmv.

3.5.3. Case 3, 21 August Over the Southeast Coast Region

On 21 August, C130 took off at the Shreveport airport at about 1450 UTC (0850 CST) and first ascended in a CO₂-rich (>410 ppmv) shallow boundary layer (<0.5 km). Then C130 flew south over the coastal area and sampled the air mass from the Gulf of Mexico. Both observation and simulation indicated CO₂ mixing ratios between 401 and 403 ppmv in the marine air mass (Figure 25b). Then C130 flew north passing the cold front mostly at >5 km above sea level and continued to fly north to the northwestern corner of Arkansas where a spiral ascent/descent was flown (Figure 25b). The model faithfully reproduces the magnitudes and vertical gradients of potential temperature and CO₂ in the free troposphere in this postfrontal environment (Figure 25b and Figure S3 in the supporting information). It also captures the boundary layer structure while slightly underestimating the boundary layer height. The model underestimates the boundary layer CO₂ mixing ratio by ~4 ppmv (simulated ~387 ppmv vs. observed ~391 ppmv).

front at ~9 km, CO₂ showed a small variation between 403 and 405 ppmv (Figure 21b). On the return path at ~5.4 km above sea level, C130 crossed the sloping front and captured the CO₂ gradient across the front with low CO₂ (as low as ~394 ppmv) behind the front and high CO₂ (as high as 404 ppmv) ahead of the front. The agreement between WRF-VPRM simulation and C130 observation is good in both horizontal and vertical cross sections (Figures 21a and 21b). The model also nicely captures the gradient of XCO₂ across the front (Figure 15c).

On the return flight before landing, C130 sampled a vertical profile over Lincoln airport at ~22 UTC. Simulated and observed profiles are compared in Figures 22a–22c, together with evaluation of simulated profiles of wind speed, potential temperature, and water vapor mixing ratio using the Radiosonde Replacement System (RRS) sounding data (downloaded from <ftp://ftp.ncdc.noaa.gov/pub/data/ua/rrs-data/>). Even though the model overestimates the boundary layer potential temperature by ~4 K, the model captures the boundary layer structure with only a slight overestimation of boundary layer height over Lincoln. A similar boundary layer structure is observed and simulated at the nearby KOAX RRS sounding site (Figures 22g–22i). The model simulation also generally captures the vertical profiles of meteorological variables at two other neighboring RRS sites, KBIS and KDVN, supporting the confidence in WRF-VPRM simulating CO₂ mixing ratio profiles. The WRF-VPRM simulation nicely captures the boundary layer-free troposphere contrast of CO₂ and boundary layer CO₂ concentration (~375 ppmv) over Lincoln (Figure 22a). The model shows a smaller variation of CO₂ in the boundary layer than C130 observation though. Such a discrepancy is partially due to the difference between PBL schemes and airplane sampling: PBL schemes are to simulate mean profile averaged over grid cells with a 12-km spacing, while airplane samples instantaneous state of the atmosphere that is affected by individual turbulent eddies, particularly during an ascent or descent, which is accomplished via spiraling up or down.

On this day, B200 also flew under OCO-2 between 1900 and 2040 UTC (see the flight track in Figure 23a). The simulated vertical cross section along the OCO-2 pass at 2000 UTC overlaid with B200 observation is shown in Figure 23b. Again, both the model and B200 indicate higher CO₂ ahead and above the sloping front and lower CO₂ behind and under

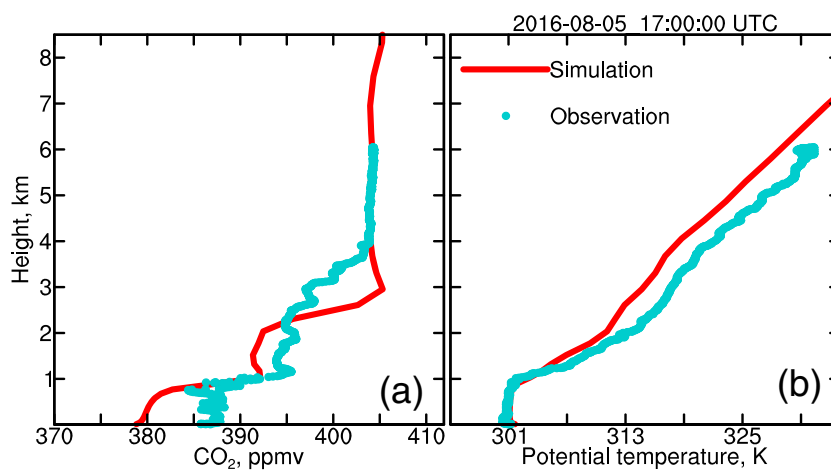


Figure 24. (a, b) Simulated profiles at 1700 UTC and observed profiles during B200 taking off at ~1715 UTC on 5 August over the Lincoln airport (40.8367°N, 96.7619°W), the southeast corner of the flight path shown on Figure 23a.

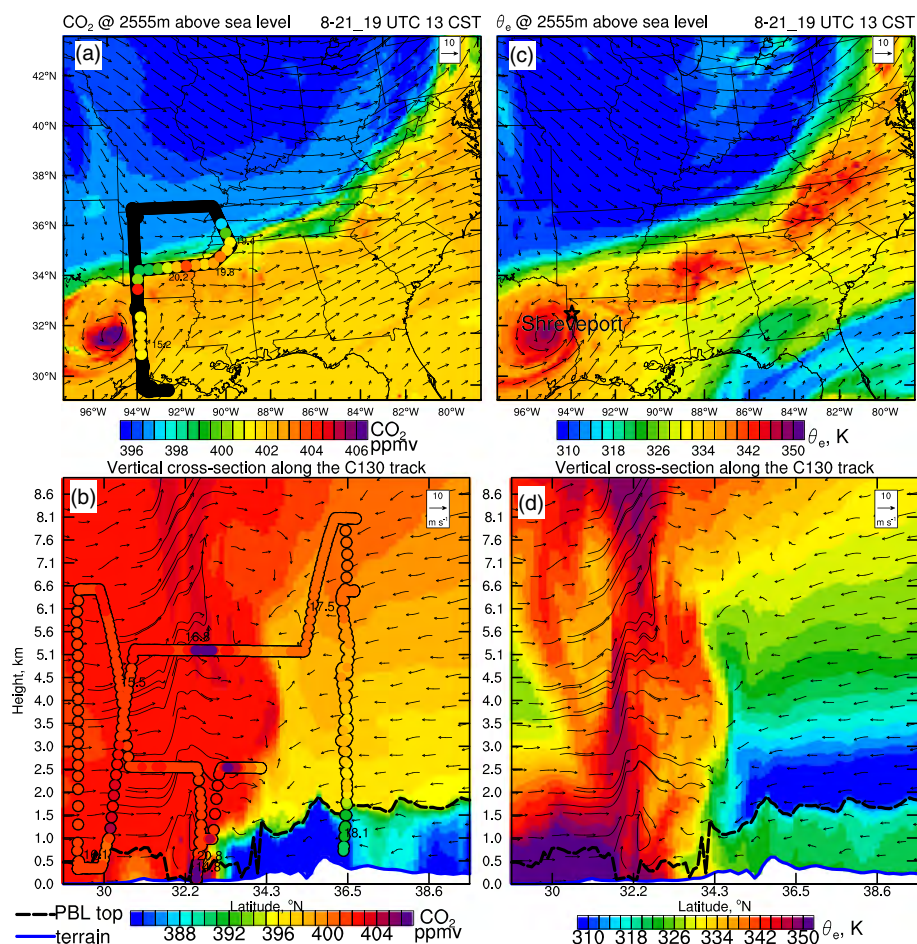


Figure 25. (a, c) Horizontal (at ~2,555 m above sea level) and (b, d) vertical cross sections of CO₂ and equivalent potential temperature (θ_e) through the straight south-north oriented flight path at 1900 UTC on 21 August simulated by WRF-VPRM, overlaid with C130 aircraft CO₂ data. Note that the flight path and CO₂ data at ~2,555 m above sea level is marked in panel (a). The UTC time is marked along the flight path. In panel (b), the data not on the straight south-north oriented flight path are not shown.

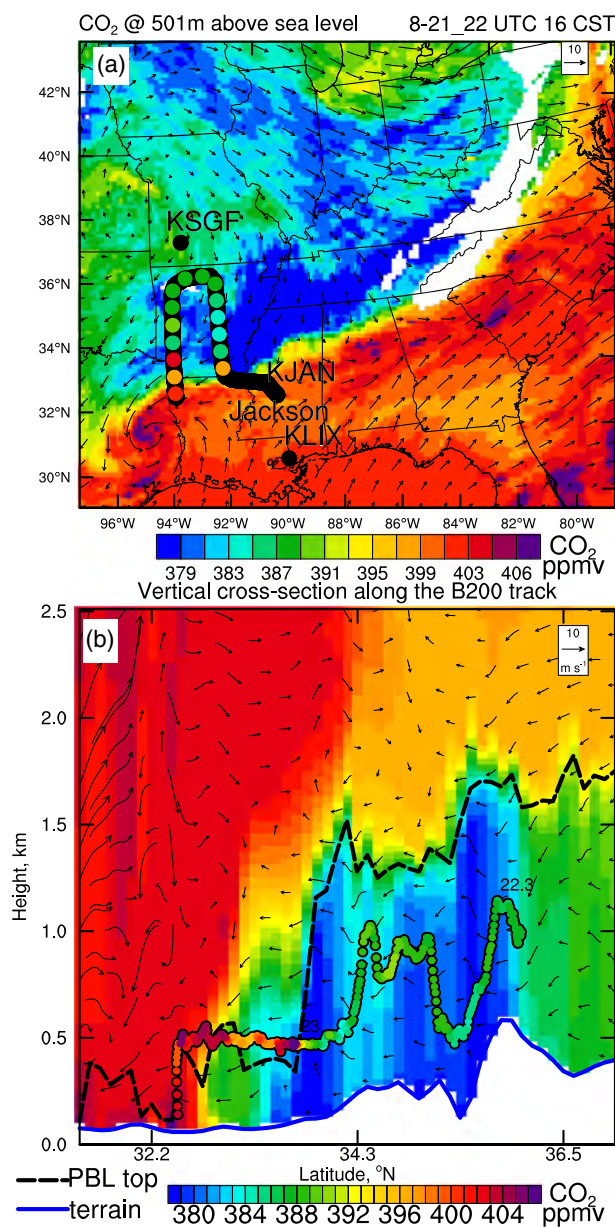


Figure 26. (a) Horizontal (at ~501 m above sea level) and (b) vertical cross sections of CO₂ through the straight south-north oriented flight path near the Texas-Louisiana border at 2200 UTC on 21 August simulated by WRF-VPRM, overlaid with B200 aircraft data. Note that the flight path and CO₂ data at ~500–1,000 m above sea level is marked in panel (a). In panel (b), the B200 data not on the left straight south-north oriented path are not shown.

The ACT-America field campaigns, which collected CO₂ and meteorological data over eastern United States in summer 2016 from multiple aircraft, as well as the spatially dense spaceborne remotely sensed column-averaged CO₂ concentrations (XCO₂) data provided by OCO-2, provided an excellent opportunity to evaluate the WRF-VPRM regional model over the CONUS domain.

In this study, calibrated VPRM parameters by Hilton et al. (2013) using eddy covariance tower data over North America were first implemented into WRF-VPRM. The updated WRF-VPRM was then used to simulate CO₂ over CONUS with a resolution of 12 km for the year 2016 in a continuous run using an optimal downscaling configuration justified in Hu, Xue, et al. (2018), with NCEP/DOE R2 and CT2017 outputs

On the return flight, C130 flew mostly at ~2.5 km above sea level and crossed the front again. Both the meteorological fields and spatial distribution of CO₂ can clearly identify the location of the cold front, which is roughly at the south border of Oklahoma (Figures 25a and 25c). C130 observations at 2,555 m above sea level captured the CO₂ gradient across the front with higher CO₂ to the south (>401 ppmv) and lower CO₂ to the north (<400 ppmv). The WRF-VPRM model nicely reproduces the cross-front gradients (Figure 25a).

Both the horizontal and vertical cross section of simulated CO₂ at 2200 UTC along with B200 observation also indicate lower CO₂ behind the cold front and higher CO₂ ahead of the front (Figure 26). The model underestimates boundary layer CO₂ behind the cold front by ~6 ppmv (simulated 379–381 ppmv vs. ~385–388 ppmv sampled by B200). At 2300 UTC B200 flew southward into the northwestern corner of Louisiana with higher CO₂ concentration (~404 ppmv). This transition of low to high CO₂ concentration captured by B200 occurs to the north of what was simulated by WRF-VPRM. This discrepancy could have two interpretations: First, the simulated front is moving southward too quickly; second, B200 intercepted some CO₂ plumes that are not simulated by the model. Figure 25a does not suggest the model simulates a too fast-moving front and thus does not support the first interpretation. There are a few emission sources from urban areas and power plants at the northeastern corner of Texas and northwestern corner of Louisiana (Hu, Xue, et al., 2019), which might have been observed by B200 under a postfront condition, but were not captured by the model.

The observed and simulated profiles at 2100 UTC when B200 took off ahead of the front are compared in Figures 27a and 27b. The model underestimate boundary layer temperature by ~3 k and overestimates boundary layer CO₂ by ~3 ppmv over Jackson. The WRF-VPRM simulation also generally captures the vertical profiles of wind speed, potential temperature, and water vapor mixing ratios over the nearby RRS sounding sites, KSGF, KJAN, and KLIX (Figures 27d–27l).

4. Discussion and Summary

Regional-scale CO₂ fluxes and subsequent CO₂ concentrations are affected by many factors including land cover and land use changes, drought, and synoptic-scale weather (e.g., midlatitude cyclones); however, the extent to which CO₂ fluxes change due to these factors remains elusive. These issues can be investigated using a weather-biosphere-online-coupled CO₂ model. One of such models, the WRF-VPRM model, was developed in ~2008 to simulate “weather-aware” biospheric CO₂ fluxes and subsequent transport/dispersion. This modeling system, however, was not rigorously evaluated over the CONUS, partially due to scarcity of appropriate observations.

Coupling the WRF-VPRM model with the CO₂ fluxes and concentrations from the ACT-America field campaigns, we evaluated the WRF-VPRM model over the CONUS domain. The results show that the WRF-VPRM model can capture the spatial distribution of CO₂ and the CO₂ fluxes over the CONUS domain. The results also show that the WRF-VPRM model can capture the CO₂ fluxes and concentrations over the CONUS domain. The results also show that the WRF-VPRM model can capture the CO₂ fluxes and concentrations over the CONUS domain.

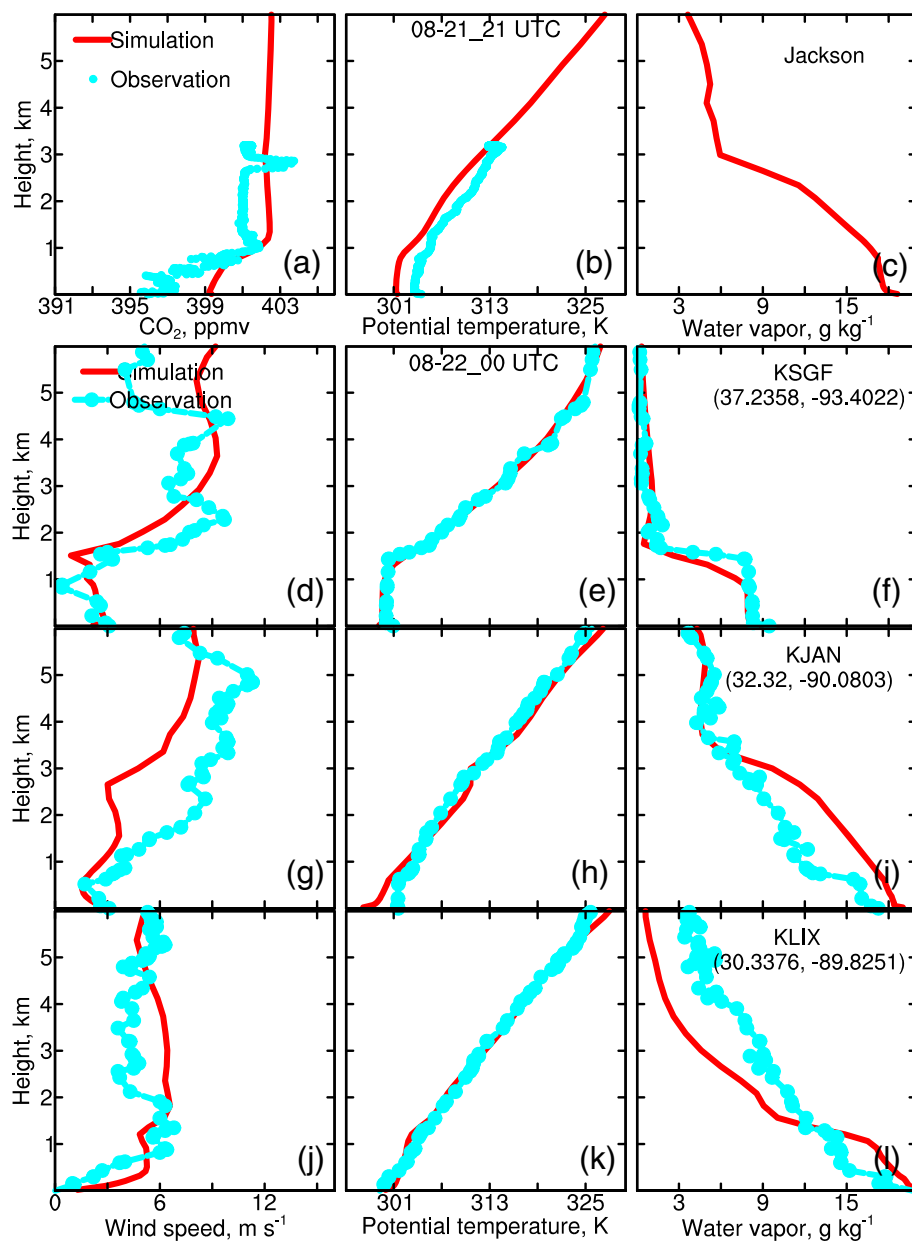


Figure 27. (a–c) Profiles of CO₂, potential temperature (θ), and water vapor mixing ratio simulated at 2100 UTC and observed during B200 taking off at ~2030 UTC on 21 August over the Jackson Airport (32.3163°N, 90.072°W), and profiles of (left to right) wind speed, θ , and water vapor mixing ratio at 0000 UTC on 22 August simulated and observed at sounding sites: (d–f) KSGF, (g–i) KJAN, and (j–l) KLIX, which are marked on Figure 26a. Note that water vapor is not available from B200 during this flight.

providing initial and boundary conditions of meteorology and CO₂, respectively. The downscaled fields are evaluated using the PRISM meteorological data and CO₂ data from OCO-2 and ACT-America, in addition to long-term surface-based XCO₂ observations from four TCCON sites (Park Falls [WI], Lamont [OK], Caltech [CA], and Dryden [CA]). Evaluation shows that meteorological downscaling is reasonably good with the model simulation capturing the location of each major frontal event throughout the year. The WRF-VPRM simulated biogenic CO₂ fluxes are compared with the CT2017 posterior fluxes, as well as SIF data. The EVI-based WRF-VPRM simulates a CO₂ sink generally consistent with the SIF data in terms of both spatial and temporal variations. Note that while the total CO₂ fluxes from CT2017 are available, biosphere fluxes from CT2017 are not partitioned into photosynthesis and respiration. Quantitative

evaluation of GEE from both WRF-VPRM and CT2017 with SIF data is warranted for future studies (Y. Zhang, Xiao, Jin, et al., 2016).

In terms of CO₂, WRF-VPRM downscaling reasonably captures monthly variation of XCO₂ and episodic variations due to frontal passages. The downscaling also successfully captures the horizontal contrast of CO₂ across fronts, as well as vertical CO₂ gradients across the boundary layer top. WRF-VPRM modeling results indicate biogenic fluxes dominate anthropogenic sources in the warm season from May to September to modulate XCO₂ over most area of CONUS except a few metropolitan areas such as Los Angeles. Note that the WRF-VPRM downscaling system is set up for the CONUS domain and the analysis is based on 1-year-long simulation in this study. The CO₂ lateral boundary condition for this limited area system is provided by the CT2017 global model data. These boundary conditions together with advection processes play a critical role in determining the CO₂ within the CONUS domain over extended period of time, especially in the free troposphere where CO₂ variation is dominated by advection processes and is less affected by surface fluxes than that in the boundary layer. Thus, the agreement of CO₂ between observations and the WRF-VPRM simulation, particularly XCO₂, is partially dictated by the CO₂ boundary conditions, from CT2017 data in this case.

The VPRM in WRF was developed about 10 years ago (Mahadevan et al., 2008). In the years afterward, the VPRM, particularly the GEE calculation, has been further improved in off-line mode by the Center for Spatial Analysis at University of Oklahoma based on improved understanding regarding the remote sensed vegetation indices and the emerging SIF measurement (Dong et al., 2015; Wagle et al., 2014; Y. Zhang, Xiao, Jin, et al., 2016; Z. C. Zhang et al., 2017). The improvement of the VPRM was made to address three issues. First, MODIS-derived EVI and Land Surface Water Index (encoded in water scalar, W_{scale}) are good representations of phenology (Xiao et al., 2009). The phenology scalar (P_{scale}) in equation 2 is redundant and unnecessary and thus is now removed. Second, the relationship between $FAPAR_{PAV}$ and EVI needs update based on the relationship between SIF and EVI (Y. Zhang, Xiao, Guanter, et al., 2016; Y. Zhang et al., 2018). Third, GEE estimation can be improved if cropland is further divided into subcategories C3 and C4 plants. The corresponding parameters for the newly updated VPRM are being calibrated using eddy covariance tower sites over North America in an off-line mode. Once the off-line calibration is finished, the newly updated VPRM and the correspondingly calibrated parameters will be incorporated into WRF in our following work.

Nevertheless, the 2016 CO₂ downscaling results over the CONUS domain reported in this manuscript demonstrate that the WRF-VPRM model can faithfully simulate impacts of some important factors (e.g., land cover spatial variation and boundary layer dynamics) on CO₂ fluxes and concentrations and thus can be used to help understand CO₂ budgets at regional to global scales (e.g., Li et al., 2020).

Acknowledgments

This study was supported by the Atmospheric Carbon and Transport (ACT)-America project through Grant NNX17AG11G at OU and grant NNX15AG76G at Penn State. The ACT-America project is a NASA Earth Venture Suborbital 2 project funded by NASA's Earth Science Division. The second author was supported by NASA OCO-2 program under Grant 80NSSC18K0896. Computations were performed at the San Diego Supercomputer Center (SDSC) through XSEDE allocation Grant

TG-ATM160014. The reanalysis data set was downloaded from the RDA website (<https://rda.ucar.edu/>), the PRISM data were downloaded from the website (<http://www.prism.oregonstate.edu/historical/>), and the CT2017 data were provided by NOAA ESRL, Boulder, Colorado, USA, from the website (<http://carbontracker.noaa.gov>).

Monthly ocean CO₂ fluxes are downloaded (from https://www.ledo.columbia.edu/res/pi/CO2/carbon dioxide/pages/air_sea_flux_2000.html).

TCCON observations are available online (<https://tccn-wiki.caltech.edu>). ACT-America data (DOI 10.3334/ORNLDAAC/1556) are downloaded from ORNL DAAC (https://daac.ornl.gov/cgi-bin/dsviewer.pl?ds_id=1556). Model data produced from this study have been archived at the oasis data server at the San Diego Supercomputer Center (/oasis/projects/nsf/uok114/xhu2/CO2_and_otherGHG).

References

- Agusti-Panareda, A., Massart, S., Chevallier, F., Boussetta, S., Balsamo, G., Beljaars, A., et al. (2014). Forecasting global atmospheric CO₂. *Atmospheric Chemistry and Physics*, 14, 11959–11983. <https://doi.org/10.5194/acp-14-11959-2014>
- Ahmadov, R., Gerbig, C., Kretschmer, R., Koerner, S., Neininger, B., Dolman, A. J., & Sarrat, C. (2007). Mesoscale covariance of transport and CO₂ fluxes: Evidence from observations and simulations using the WRF-VPRM coupled atmosphere-biosphere model. *Journal of Geophysical Research*, 112, D22107. <https://doi.org/10.1029/2007JD008552>
- Ahmadov, R., Gerbig, C., Kretschmer, R., Korner, S., Rodenbeck, C., Bousquet, P., & Ramonet, M. (2009). Comparing high resolution WRF-VPRM simulations and two global CO₂ transport models with coastal tower measurements of CO₂. *Biogeosciences*, 6(5), 807–817.
- Anav, A., Friedlingstein, P., Beer, C., Ciais, P., Harper, A., Jones, C., et al. (2015). Spatiotemporal patterns of terrestrial gross primary production: A review. *Reviews of Geophysics*, 53(3), 785–818. <https://doi.org/10.1002/2015RG000483>
- Baldocchi, D., Ryu, Y., & Keenan, T. (2016). Terrestrial carbon cycle variability [version 1; referees: 2 approved] (Vol. 5).
- Basu, S., Guerlet, S., Butz, A., Houweling, S., Hasekamp, O., Aben, I., et al. (2013). Global CO₂ fluxes estimated from GOSAT retrievals of total column CO₂. *Atmospheric Chemistry and Physics*, 13(17), 8695–8717. <https://doi.org/10.5194/acp-13-8695-2013>
- Bie, N., Lei, L. P., Zeng, Z. C., Cai, B. F., Yang, S. Y., He, Z. H., et al. (2018). Regional uncertainty of GOSAT XCO₂ retrievals in China: Quantification and attribution. *Atmospheric Measurement Techniques*, 11(3), 1251–1272. <https://doi.org/10.5194/amt-11-1251-2018>
- Braendholt, A., Ibrom, A., Larsen, K. S., & Pilegaard, K. (2018). Partitioning of ecosystem respiration in a beech forest. *Agricultural and Forest Meteorology*, 252, 88–98. <https://doi.org/10.1016/j.agrformet.2018.01.012>
- Chan, D., Yuen, C. W., Higuchi, K., Shashkov, A., Liu, J., Chen, J., & Worthy, D. (2004). On the CO₂ exchange between the atmosphere and the biosphere: The role of synoptic and mesoscale processes. *Tellus Series B: Chemical and Physical Meteorology*, 56(3), 194–212. <https://doi.org/10.1111/j.1600-0889.2004.00104.x>
- Chen, F., & Dudhia, J. (2001). Coupling an advanced land surface-hydrology model with the Penn State-NCAR MM5 modeling system. Part I: Model implementation and sensitivity. *Monthly Weather Review*, 129(4), 569–585. [https://doi.org/10.1175/1520-0493\(2001\)129<0569:Caalsh>2.0.Co;2](https://doi.org/10.1175/1520-0493(2001)129<0569:Caalsh>2.0.Co;2)

- Chen, H. W., Zhang, L. N., Zhang, F., Davis, K. J., Lauvaux, T., Pal, S., et al. (2019). Evaluation of regional CO₂ mole fractions in the ECMWF CAMS real-time atmospheric analysis and NOAA CarbonTracker Near-Real-Time reanalysis with airborne observations from ACT-America field campaigns. *Journal of Geophysical Research-Atmospheres*, *124*, 8119–8133. <https://doi.org/10.1029/2018JD029992>
- Connor, B. J., Boesch, H., Toon, G., Sen, B., Miller, C., & Crisp, D. (2008). Orbiting carbon observatory: Inverse method and prospective error analysis. *Journal of Geophysical Research*, *113*, D05305. <https://doi.org/10.1029/2006JD008336>
- Crisp, D., Atlas, R. M., Breon, F. M., Brown, L. R., Burrows, J. P., Ciais, P., et al. (2004). The orbiting carbon observatory (OCO) mission. *Trace Constituents in the Troposphere and Lower Stratosphere*, *34*(4), 700–709. <https://doi.org/10.1016/j.asr.2003.08.062>
- Crisp, D., Miller, C. E., & DeCola, P. L. (2008). NASA Orbiting Carbon Observatory: Measuring the column averaged carbon dioxide mole fraction from space. *Journal of Applied Remote Sensing*, *2*, 023508. <https://doi.org/10.1117/1.2898457>
- Dai, A., Giorgi, F., & Trenberth, K. E. (1999). Observed and model-simulated diurnal cycles of precipitation over the contiguous United States. *Journal of Geophysical Research*, *104*(D6), 6377–6402. <https://doi.org/10.1029/98JD02720>
- Daly, C., Neilson, R. P., & Phillips, D. L. (1994). A statistical topographic model for mapping climatological precipitation over mountainous terrain. *Journal of Applied Meteorology*, *33*(2), 140–158. [https://doi.org/10.1175/1520-0450\(1994\)033<0140:Astfm>2.0.Co;2](https://doi.org/10.1175/1520-0450(1994)033<0140:Astfm>2.0.Co;2)
- Diao, Y., Huang, J., Liu, C., Cui, J., & Liu, S. (2015). A modeling study of CO₂ flux and concentrations over the Yangtze River Delta using the WRF-GHG model. (in Chinese). *Chinese Journal of Atmospheric Sciences*, *39*(5), 849–860.
- Diaz-Isaac, L. I., Lauvaux, T., & Davis, K. J. (2018). Impact of physical parameterizations and initial conditions on simulated atmospheric transport and CO₂ mole fractions in the US Midwest. *Atmospheric Chemistry and Physics*, *18*(20), 14813–14835. <https://doi.org/10.5194/acp-18-14813-2018>
- Diaz-Isaac, L. I., Lauvaux, T., Davis, K. J., Miles, N. L., Richardson, S. J., Jacobson, A. R., & Andrews, A. E. (2014). Model-data comparison of MCI field campaign atmospheric CO₂ mole fractions. *Journal of Geophysical Research-Atmospheres*, *119*, 10536–10551. <https://doi.org/10.1002/2014JD021593>
- Digangi, J. P., Choi, Y., Nowak, J. B., Halliday, H. S., & Yang, M. M. (2018). ACT-America: L2 in situ atmospheric CO₂, CO, CH₄, and O₃ concentrations, Eastern USA. Retrieved from: https://daac.ornl.gov/cgi-bin/dsviewer.pl?ds_id=1556
- Dils, B., Buchwitz, M., Reuter, M., Schneising, O., Boesch, H., Parker, R., et al. (2014). The Greenhouse Gas Climate Change Initiative (GHG-CCI): Comparative validation of GHG-CCI SCIAMACHY/ENVISAT and TANSO-FTS/GOSAT CO₂ and CH₄ retrieval algorithm products with measurements from the TCCON. *Atmospheric Measurement Techniques*, *7*(6), 1723–1744. <https://doi.org/10.5194/amt-7-1723-2014>
- Dong, J. W., Xiao, X. M., Wagle, P., Zhang, G. L., Zhou, Y. T., Jin, C., et al. (2015). Comparison of four EVI-based models for estimating gross primary production of maize and soybean croplands and tallgrass prairie under severe drought. *Remote Sensing of Environment*, *162*, 154–168. <https://doi.org/10.1016/j.rse.2015.02.022>
- Dudhia, J. (1989). Numerical study of convection observed during the Winter Monsoon Experiment using a mesoscale two-dimensional model. *Journal of the Atmospheric Sciences*, *46*(20), 3077–3107. [https://doi.org/10.1175/1520-0469\(1989\)046<3077:Nsocod>2.0.Co;2](https://doi.org/10.1175/1520-0469(1989)046<3077:Nsocod>2.0.Co;2)
- Easterling, D. R., Meehl, G. A., Parmesan, C., Changnon, S. A., Karl, T. R., & Mearns, L. O. (2000). Climate extremes: Observations, modeling, and impacts. *Science*, *289*(5487), 2068–2074. <https://doi.org/10.1126/science.289.5487.2068>
- Elderling, A., O'Dell, C. W., Wennberg, P. O., Crisp, D., Gunson, M. R., Viatte, C., et al. (2017). The Orbiting Carbon Observatory-2: First 18 months of science data products. *Atmospheric Measurement Techniques*, *10*(2), 549–563. <https://doi.org/10.5194/amt-10-549-2017>
- Feng, S., Lauvaux, T., Newman, S., Rao, P., Ahmadov, R., Deng, A. J., et al. (2016). Los Angeles megacity: a high-resolution land-atmosphere modelling system for urban CO₂ emissions. *Atmospheric Chemistry and Physics*, *16*(14), 9019–9045. <https://doi.org/10.5194/acp-16-9019-2016>
- Findell, K. L., Gentine, P., Lintner, B. R., & Kerr, C. (2011). Probability of afternoon precipitation in eastern United States and Mexico enhanced by high evaporation. *Nature Geoscience*, *4*(7), 434–439. <https://doi.org/10.1038/Ngeo1174>
- Forkel, M., Carvalhais, N., Rödenbeck, C., Keeling, R., Heimann, M., Thonicke, K., et al. (2016). Enhanced seasonal CO₂ exchange caused by amplified plant productivity in northern ecosystems. *Science*, *351*(6274), 696–699. <https://doi.org/10.1126/science.aac4971>
- Graven, H. D., Keeling, R. F., Piper, S. C., Patra, P. K., Stephens, B. B., Wofsy, S. C., et al. (2013). Enhanced seasonal exchange of CO₂ by northern ecosystems since 1960. *Science*, *341*(6150), 1085–1089. <https://doi.org/10.1126/science.1239207>
- Grell, G. A., & Devenyi, D. (2002). A generalized approach to parameterizing convection combining ensemble and data assimilation techniques. *Geophysical Research Letters*, *29*(14), 1693. <https://doi.org/10.1029/2002gl015311>
- Hilton, T. W., Davis, K. J., & Keller, K. (2014). Evaluating terrestrial CO₂ flux diagnoses and uncertainties from a simple land surface model and its residuals. *Biogeosciences*, *11*(2), 217–235. <https://doi.org/10.5194/bg-11-217-2014>
- Hilton, T. W., Davis, K. J., Keller, K., & Urban, N. M. (2013). Improving North American terrestrial CO₂ flux diagnosis using spatial structure in land surface model residuals. *Biogeosciences*, *10*(7), 4607–4625. <https://doi.org/10.5194/bg-10-4607-2013>
- Hilton, T. W., Davis, K. J., Keller, K., & Urban, N. M. (2016). NACP VPRM NEE parameters optimized to North American flux tower sites, 2000–2006. Retrieved from: [http://daac.ornl.gov/cgi-bin/dsviewer.pl?ds_id=1349](https://daac.ornl.gov/cgi-bin/dsviewer.pl?ds_id=1349)
- Hu, X.-M. (2008). Incorporation of the Model of Aerosols Dynamics, Reaction, Ionization, and Dissolution (MADRID) into the Weather Research and Forecasting Model with Chemistry (WRF/Chem): Model development and retrospective applications. (PhD thesis), NC State Univ. Retrieved from <http://repository.lib.ncsu.edu/ir/handle/1840.16/5241>
- Hu, X.-M., Crowell, S., Wang, Q., Zhang, Y., Xue, M., Xiao, X., et al. (2018). CO₂ dynamical downscaling in 2016 over the contiguous United States using WRF-VPRM, a weather-biosphere-online-coupled model. Paper presented at the AGU's Fall Meeting Washington, D.C.. <https://agu.confex.com/agu/fm18/meetingapp.cgi/Paper/351893>
- Hu, X.-M., Doughty, D. C., Sanchez, K. J., Joseph, E., & Fuentes, J. D. (2012). Ozone variability in the atmospheric boundary layer in Maryland and its implications for vertical transport model. *Atmospheric Environment*, *46*, 354–364. <https://doi.org/10.1016/j.atmosenv.2011.09.054>
- Hu, X.-M., Klein, P. M., & Xue, M. (2013). Evaluation of the updated YSU planetary boundary layer scheme within WRF for wind resource and air quality assessments. *Journal of Geophysical Research-Atmospheres*, *118*(18), 10490–10505. <https://doi.org/10.1002/jgrd.50823>
- Hu, X.-M., Nielsen-Gammon, J. W., & Zhang, F. Q. (2010). Evaluation of three planetary boundary layer schemes in the WRF model. *Journal of Applied Meteorology and Climatology*, *49*(9), 1831–1844. <https://doi.org/10.1175/2010jamc2432.1>
- Hu, X.-M., Wang, Q., Crowell, S., Zhang, Y., Xue, M., Xiao, X., et al. (2019). CO₂ dynamical downscaling in 2016 over the contiguous United States using WRF-VPRM, a weather-biosphere-online-coupled model. Paper presented at the 99th AMS Annual Meeting, Phoenix, AZ <https://ams.confex.com/ams/2019Annual/meetingapp.cgi/Paper/354045>

- Hu, X.-M., Xue, M., Kong, F. Y., & Zhang, H. L. (2019). Meteorological conditions during an ozone episode in Dallas-Fort Worth, Texas, and impact of their modeling uncertainties on air quality prediction. *Journal of Geophysical Research-Atmospheres*, 124, 1941–1961. <https://doi.org/10.1029/2018JD029791>
- Hu, X.-M., Xue, M., & McPherson, R. A. (2017). The importance of soil-type contrast in modulating August precipitation distribution near the Edwards Plateau and Balcones Escarpment in Texas. *Journal of Geophysical Research-Atmospheres*, 122, 10711–10728. <https://doi.org/10.1002/2017JD027035>
- Hu, X.-M., Xue, M., McPherson, R. A., Martin, E., Rosendahl, D. H., & Qiao, L. (2018). Precipitation dynamical downscaling over the Great Plains. *Journal of Advances in Modeling Earth Systems*, 10, 421–447. <https://doi.org/10.1002/2017MS001154>
- Hu, X.-M., Zhang, Y., Crowell, S., Xue, M., Moore, B., Xiao, X., et al. (2018). Evaluation of WRF-VPRM CO₂ dynamical downscaling over the contiguous United States using the ACT-America Data. Paper presented at the 98th annual meeting of American Meteorological Society, Austin. <https://ams.confex.com/ams/98Annual/meetingapp.cgi/Paper/333148>
- Huntzinger, D. N., Schwalm, C. R., Wei, Y., Cook, R. B., Michalak, A. M., Schaefer, K., et al. (2018). NACP MsTMIP: Global 0.5-degree model outputs in standard format, Version 1.0: ORNL Distributed Active Archive Center, doi: <https://doi.org/10.3334/ornl daac/1225>.
- Hurwitz, M. D., Ricciuto, D. M., Bakwin, P. S., Davis, K. J., Wang, W. G., Yi, C. X., & Butler, M. P. (2004). Transport of carbon dioxide in the presence of storm systems over a Northern Wisconsin forest. *Journal of the Atmospheric Sciences*, 61(5), 607–618. [https://doi.org/10.1175/1520-0469\(2004\)061<0607:Tocdit>2.0.CO;2](https://doi.org/10.1175/1520-0469(2004)061<0607:Tocdit>2.0.CO;2)
- Janjic, Z. I. (1990). The step-mountain coordinate: Physical package. *Monthly Weather Review*, 118(7), 1429–1443. [https://doi.org/10.1175/1520-0493\(1990\)118<1429:TSMCPP>2.0.CO;2](https://doi.org/10.1175/1520-0493(1990)118<1429:TSMCPP>2.0.CO;2)
- Janjic, Z. I. (1994). The step-mountain eta coordinate model—Further developments of the convection, viscous sublayer, and turbulence closure schemes. *Monthly Weather Review*, 122(5), 927–945. [https://doi.org/10.1175/1520-0493\(1994\)122<0927:Tsmech>2.0.CO;2](https://doi.org/10.1175/1520-0493(1994)122<0927:Tsmech>2.0.CO;2)
- Kanamitsu, M., Ebisuzaki, W., Woollen, J., Yang, S. K., Hnilo, J. J., Fiorino, M., & Potter, G. L. (2002). NCEP-DOE AMIP-II reanalysis (R-2). *Bulletin of the American Meteorological Society*, 83(11), 1631–1643. <https://doi.org/10.1175/Bams-83-11-1631>
- Kiel, M., O'Dell, C. W., Fisher, B., Elderling, A., Nassar, R., MacDonald, C. G., & Wennberg, P. O. (2019). How bias correction goes wrong: measurement of X-CO₂ affected by erroneous surface pressure estimates. *Atmospheric Measurement Techniques*, 12(4), 2241–2259. <https://doi.org/10.5194/amt-12-2241-2019>
- Knapp, A. K., & Smith, M. D. (2001). Variation among biomes in temporal dynamics of aboveground primary production. *Science*, 291(5503), 481–484. <https://doi.org/10.1126/science.291.5503.481>
- Krause, G. H., & Weis, E. (1991). Chlorophyll fluorescence and photosynthesis—The basics. *Annual Review of Plant Physiology and Plant Molecular Biology*, 42, 313–349. <https://doi.org/10.1146/annurev.pp.42.060191.001525>
- Lark, T. J., Mueller, R. M., Johnson, D. M., & Gibbs, H. K. (2017). Measuring land-use and land-cover change using the U.S. Department of Agriculture's cropland data layer: Cautions and recommendations. *International Journal of Applied Earth Observation and Geoinformation*, 62(Supplement C), 224–235. <https://doi.org/10.1016/j.jag.2017.06.007>
- Lauvaux, T., Schuh, A. E., Uljasz, M., Richardson, S., Miles, N., Andrews, A. E., et al. (2012). Constraining the CO₂ budget of the corn belt: Exploring uncertainties from the assumptions in a mesoscale inverse system. *Atmospheric Chemistry and Physics*, 12(1), 337–354. <https://doi.org/10.5194/acp-12-337-2012>
- Leibensperger, E. M., Mickley, L. J., & Jacob, D. J. (2008). Sensitivity of US air quality to mid-latitude cyclone frequency and implications of 1980–2006 climate change. *Atmospheric Chemistry and Physics*, 8(23), 7075–7086.
- Li, X., Hu, X.-M., Cai, C., Jia, Q., Zhang, Y., Liu, J., et al. (2020). Terrestrial CO₂ fluxes, concentrations, sources and budget in Northeast China: Observational and modeling studies. *Journal of Geophysical Research: Atmospheres*, 125, e2019JD031686. <https://doi.org/10.1029/2019JD031686>
- Liang, X. Z., Pan, J. P., Zhu, J. H., Kunkel, K. E., Wang, J. X. L., & Dai, A. (2006). Regional climate model downscaling of the U.S. summer climate and future change. *Journal of Geophysical Research*, 111, D10108. <https://doi.org/10.1029/2005JD006685>
- Liu, Y., Yue, T., Zhang, L., Zhao, N., Zhao, M., & Liu, Y. (2018). Simulation and analysis of XCO₂ in North China based on high accuracy surface modeling. *Environmental Science and Pollution Research*, 25(27), 27378–27392. <https://doi.org/10.1007/s11356-018-2683-x>
- Mahadevan, P., Wofsy, S. C., Matross, D. M., Xiao, X. M., Dunn, A. L., Lin, J. C., et al. (2008). A satellite-based biosphere parameterization for net ecosystem CO₂ exchange: Vegetation Photosynthesis and Respiration Model (VPRM). *Global Biogeochemical Cycles*, 22, GB2005. <https://doi.org/10.1029/2006GB002735>
- Martynov, A., Laprise, R., Sushama, L., Winger, K., Separovic, L., & Dugas, B. (2013). Reanalysis-driven climate simulation over CORDEX North America domain using the Canadian Regional Climate Model, version 5: Model performance evaluation. *Climate Dynamics*, 41(11–12), 2973–3005. <https://doi.org/10.1007/s00382-013-1778-9>
- Mearns, L. O., Arritt, R., Biner, S., Bukovsky, M. S., McGinnis, S., Sain, S., et al. (2012). The North American Regional Climate Change Assessment Program: Overview of Phase I results. *Bulletin of the American Meteorological Society*, 93(9), 1337–1362. <https://doi.org/10.1175/BAMS-D-11-00223.1>
- Miao, R., Lu, N., Yao, L., Zhu, Y. Q., Wang, J. L., & Sun, J. L. (2013). Multi-year comparison of carbon dioxide from satellite data with ground-based FTS measurements (2003–2011). *Remote Sensing*, 5(7), 3431–3456.
- Migliavacca, M., Reichstein, M., Richardson, A. D., Colombo, R., Sutton, M. A., Lasslop, G., et al. (2011). Semiempirical modeling of abiotic and biotic factors controlling ecosystem respiration across eddy covariance sites. *Global Change Biology*, 17(1), 390–409. <https://doi.org/10.1111/j.1365-2486.2010.02243.x>
- Miles, N. L., Richardson, S. J., Davis, K. J., Lauvaux, T., Andrews, A. E., West, T. O., et al. (2012). Large amplitude spatial and temporal gradients in atmospheric boundary layer CO₂ mole fractions detected with a tower-based network in the U.S. upper Midwest. *Journal of Geophysical Research*, 117, G01019. <https://doi.org/10.1029/2011JG001781>
- Mlawer, E. J., Taubman, S. J., Brown, P. D., Iacono, M. J., & Clough, S. A. (1997). Radiative transfer for inhomogeneous atmospheres: RRTM, a validated correlated-k model for the longwave. *Journal of Geophysical Research-Atmospheres*, 102(D14), 16663–16682. <https://doi.org/10.1029/97jd00237>
- Morrison, H., Thompson, G., & Tatarskii, V. (2009). Impact of cloud microphysics on the development of trailing stratiform precipitation in a simulated squall line: Comparison of one- and two-moment schemes. *Monthly Weather Review*, 137(3), 991–1007. <https://doi.org/10.1175/2008mwr2556.1>
- Neild, R. E., & Newman, J. E. (1987). *Growing season characteristics and requirements in the corn belt*. Ames, Iowa: Cooperative Extension Service, Iowa State University. <https://www.extension.purdue.edu/extmedia/NCH/NCH-40.html>
- Oda, T., Maksyutov, S., & Andres, R. J. (2018). The Open-source Data Inventory for Anthropogenic CO₂, version 2016 (ODIAC2016): A global monthly fossil fuel CO₂ gridded emissions data product for tracer transport simulations and surface flux inversions. *Earth System Science Data*, 10(1), 87–107. <https://doi.org/10.5194/essd-10-87-2018>

- Pal, S., Davis, K. J., Lauvaux, T., Browell, E. V., Gaudet, B. J., Stauffer, D. R., et al. (2020). Observations of greenhouse gas changes across summer frontal boundaries in the eastern United States. *Journal of Geophysical Research*, 125(5). <https://doi.org/10.1029/2019JD030526>
- Parazoo, N. C., Denning, A. S., Berry, J. A., Wolf, A., Randall, D. A., Kawa, S. R., et al. (2011). Moist synoptic transport of CO₂ along the mid-latitude storm track. *Geophysical Research Letters*, 38, L09804. <https://doi.org/10.1029/2011GL047238>
- Park, C., Gerbig, C., Newman, S., Ahmadov, R., Feng, S., Gurney, K. R., et al. (2018). CO₂ transport, variability, and budget over the Southern California air basin using the high-resolution WRF-VPRM model during the CalNex 2010 campaign. *Journal of Applied Meteorology and Climatology*, 57(6), 1337–1352. <https://doi.org/10.1175/jamc-d-17-0358.1>
- Peters, W., Jacobson, A. R., Sweeney, C., Andrews, A. E., Conway, T. J., Masarie, K., et al. (2007). An atmospheric perspective on North American carbon dioxide exchange: CarbonTracker. *Proceedings of the National Academy of Sciences of the United States of America*, 104(48), 18925–18930. <https://doi.org/10.1073/pnas.0708986104>
- Petrescu, A. M. R., Abad-Vinas, R., Janssens-Maenhout, G., Blujdea, V. N. B., & Grassi, G. (2012). Global estimates of carbon stock changes in living forest biomass: EDGARv4.3-time series from 1990 to 2010. *Biogeosciences*, 9(8), 3437–3447. <https://doi.org/10.5194/bg-9-3437-2012>
- Pillai, D., Gerbig, C., Ahmadov, R., Rodenbeck, C., Kretschmer, R., Koch, T., et al. (2011). High-resolution simulations of atmospheric CO₂ over complex terrain—Representing the Ochsenkopf mountain tall tower. *Atmospheric Chemistry and Physics*, 11(15), 7445–7464. <https://doi.org/10.5194/acp-11-7445-2011>
- Prat, O. P., & Nelson, B. R. (2015). Evaluation of precipitation estimates over CONUS derived from satellite, radar, and rain gauge data sets at daily to annual scales (2002–2012). *Hydrology and Earth System Sciences*, 19(4), 2037–2056. <https://doi.org/10.5194/hess-19-2037-2015>
- Qiao, F. X., & Liang, X. Z. (2015). Effects of cumulus parameterizations on predictions of summer flood in the Central United States. *Climate Dynamics*, 45(3–4), 727–744. <https://doi.org/10.1007/s00382-014-2301-7>
- Racza, B. M., Davis, K. J., Huntzinger, D., Neilson, R. P., Poulter, B., Richardson, A. D., et al. (2013). Evaluation of continental carbon cycle simulations with North American flux tower observations. *Ecological Monographs*, 83(4), 531–556. <https://doi.org/10.1890/12-0893.1>
- Reichstein, M., Bahn, M., Ciais, P., Frank, D., Mahecha, M. D., Seneviratne, S. I., et al. (2013). Climate extremes and the carbon cycle. *Nature*, 500(7462), 287–295. <https://doi.org/10.1038/nature12350>
- Schumacher, R. S., Clark, A. J., Xue, M., & Kong, F. Y. (2013). Factors influencing the development and maintenance of nocturnal heavy-rain-producing convective systems in a storm-scale ensemble. *Monthly Weather Review*, 141(8), 2778–2801. <https://doi.org/10.1175/MWR-D-12-00239.1>
- Seigneur, C., Pun, B., Pai, P., Louis, J. F., Solomon, P., Emery, C., et al. (2000). Guidance for the performance evaluation of three-dimensional air quality modeling systems for particulate matter and visibility. *Journal of the Air & Waste Management Association*, 50(4), 588–599. <https://doi.org/10.1080/10473289.2000.10464036>
- Song, L., Zhang, Y., & Qian, X. (2016). Fusion of SCIAMACHY and GOME-2 satellite Sun-induced fluorescence data. Paper presented at the 2016 IEEE International Geoscience and Remote Sensing Symposium (IGARSS).
- Sun, X., Xue, M., Brotzge, J., McPherson, R. A., Hu, X.-M., & Yang, X.-Q. (2016). An evaluation of dynamical downscaling of Central Plains summer precipitation using a WRF-based regional climate model at a convection-permitting 4 km resolution. *Journal of Geophysical Research-Atmospheres*, 121, 13,801–813,825. <https://doi.org/10.1002/2016JD024796>
- Sun, Y., Frankenberg, C., Jung, M., Joiner, J., Guanter, L., Kohler, P., & Magney, T. (2018). Overview of solar-induced chlorophyll fluorescence (SIF) from the Orbiting Carbon Observatory-2: Retrieval, cross-mission comparison, and global monitoring for GPP. *Remote Sensing of Environment*, 209, 808–823. <https://doi.org/10.1016/j.rse.2018.02.016>
- Takahashi, T., Sutherland, S. C., Wanninkhof, R., Sweeney, C., Feely, R. A., Chipman, D. W., et al. (2009). Climatological mean and decadal change in surface ocean pCO₂, and net sea-air CO₂ flux over the global oceans. *Deep-Sea Research Part Ii-Topical Studies in Oceanography*, 56(8–10), 554–577. <https://doi.org/10.1016/j.dsr.2008.12.009>
- Tang, J. W., Bolstad, P. V., Desai, A. R., Martin, J. G., Cook, B. D., Davis, K. J., & Carey, E. V. (2008). Ecosystem respiration and its components in an old-growth forest in the Great Lakes region of the United States. *Agricultural and Forest Meteorology*, 148(2), 171–185. <https://doi.org/10.1016/j.agrformet.2007.08.008>
- Wagle, P., Xiao, X. M., Torn, M. S., Cook, D. R., Matamala, R., Fischer, M. L., et al. (2014). Sensitivity of vegetation indices and gross primary production of tallgrass prairie to severe drought. *Remote Sensing of Environment*, 152, 1–14. <https://doi.org/10.1016/J.Rse.2014.05.010>
- Wang, J., Xiao, X. M., Qin, Y. W., Dong, J. W., Geissler, G., Zhang, G. L., et al. (2017). Mapping the dynamics of eastern redcedar encroachment into grasslands during 1984–2010 through PALSAR and time series Landsat images. *Remote Sensing of Environment*, 190, 233–246. <https://doi.org/10.1016/j.rse.2016.12.025>
- Wang, J. L., & Kotamarthi, V. R. (2013). Assessment of dynamical downscaling in near-surface fields with different spectral nudging approaches using the Nested Regional Climate Model (NRCM). *Journal of Applied Meteorology and Climatology*, 52(7), 1576–1591. <https://doi.org/10.1175/Jamc-D-12-0302.1>
- Wang, J. L., & Kotamarthi, V. R. (2014). Downscaling with a nested regional climate model in near-surface fields over the contiguous United States. *Journal of Geophysical Research-Atmospheres*, 119, 8778–8797. <https://doi.org/10.1002/2014JD021696>
- Wunch, D., Wennberg, P. O., Osterman, G., Fisher, B., Naylor, B., Roehl, C. M., et al. (2017). Comparisons of the Orbiting Carbon Observatory-2 (OCO-2) X-CO₂ measurements with TCCON. *Atmospheric Measurement Techniques*, 10(6), 2209–2238. <https://doi.org/10.5194/amt-10-2209-2017>
- Xiao, X., Zhang, J.-H., Yan, H., Wu, W., & Biradar, C. (2009). *Land surface phenology: Convergence of satellite and CO₂ eddy flux observations*. In *Phenology of Ecosystem Processes* (ed. Noormets A), (pp. 247–270). New York: Springer.
- Xiao, X. M., Hollinger, D., Aber, J., Goltz, M., Davidson, E. A., Zhang, Q. Y., & Moore, B. (2004). Satellite-based modeling of gross primary production in an evergreen needleleaf forest. *Remote Sensing of Environment*, 89(4), 519–534. <https://doi.org/10.1016/j.rse.2003.11.008>
- Zeng, N., Zhao, F., Collatz, G. J., Kalmay, E., Salawitch, R. J., West, T. O., & Guanter, L. (2014). Agricultural Green Revolution as a driver of increasing atmospheric CO₂ seasonal amplitude. *Nature*, 515, 394. <https://doi.org/10.1038/nature13893>
- Zeng, Z. C., Lei, L. P., Strong, K., Jones, D. B. A., Guo, L. J., Liu, M., et al. (2017). Global land mapping of satellite-observed CO₂ total columns using spatio-temporal geostatistics. *International Journal of Digital Earth*, 10(4), 426–456. <https://doi.org/10.1080/17538947.2016.1156777>
- Zhang, F. M., & Pu, Z. X. (2019). Sensitivity of numerical simulations of near-surface atmospheric conditions to snow depth and surface albedo during an ice fog event over Heber Valley. *Journal of Applied Meteorology and Climatology*, 58(4), 797–811. <https://doi.org/10.1175/Jamc-D-18-0064.1>

- Zhang, Y., Xiao, X., Guanter, L., Zhou, S., Ciais, P., Joiner, J., et al. (2016). Precipitation and carbon-water coupling jointly control the interannual variability of global land gross primary production. *Scientific Reports*, 6(1), 39748. <https://doi.org/10.1038/srep39748>
- Zhang, Y., Xiao, X. M., Jin, C., Dong, J. W., Zhou, S., Wagle, P., et al. (2016). Consistency between Sun-induced chlorophyll fluorescence and gross primary production of vegetation in North America. *Remote Sensing of Environment*, 183, 154–169. <https://doi.org/10.1016/j.rse.2016.05.015>
- Zhang, Y., Xiao, X. M., Wolf, S., Wu, J., Wu, X. C., Gioli, B., et al. (2018). Spatio-temporal convergence of maximum daily light-use efficiency based on radiation absorption by canopy chlorophyll. *Geophysical Research Letters*, 45, 3508–3519. <https://doi.org/10.1029/2017GL076354>
- Zhang, Y., Xiao, X. M., Wu, X. C., Zhou, S., Zhang, G. L., Qin, Y. W., & Dong, J. W. (2017). Data descriptor: A global moderate resolution dataset of gross primary production of vegetation for 2000–2016. *Scientific Data*, 4, 170165. <https://doi.org/10.1038/sdata.2017.165>
- Zhou, Y. T., Xiao, X. M., Zhang, G. L., Wagle, P., Bajgain, R., Dong, J. W., et al. (2017). Quantifying agricultural drought in tallgrass prairie region in the US Southern Great Plains through analysis of a water-related vegetation index from MODIS images. *Agricultural and Forest Meteorology*, 246, 111–122. <https://doi.org/10.1016/j.agrformet.2017.06.007>
- Zscheischler, J., Reichstein, M., von Buttlar, J., Mu, M., Randerson, J. T., & Mahecha, M. D. (2014). Carbon cycle extremes during the 21st century in CMIP5 models: Future evolution and attribution to climatic drivers. *Geophysical Research Letters*, 41, 8853–8861. <https://doi.org/10.1002/2014GL062409>